Chaos

Ordered intricacy of Shilnikov saddle-focus homoclinics in symmetric systems (F)

Tingli Xing, (iD) Krishna Pusuluri, and (iD) Andrey L. Shilnikov

COLLECTIONS

Note: This paper is part of the Focus Issue, Global Bifurcations, Chaos, and Hyperchaos: Theory and Applications.

(F) This paper was selected as Featured

View Online   Export Citation   CrossMark

Ordered intricacy of Shilnikov saddle-focus homoclinics in symmetric systems Ⓕ

View Online   Export Citation   CrossMark

Tingli Xing,[1,a)] Krishna Pusuluri,[2,3,b)] and Andrey L. Shilnikov[1,3,c)]

AFFILIATIONS

[1]Department of Mathematics and Statistics, Georgia State University, Atlanta, Georgia 30303, USA
[2]Department of Biology, Emory University, Atlanta, Georgia 30322, USA
[3]Neuroscience Institute, Georgia State University, Atlanta, Georgia 30303, USA

Note: This paper is part of the Focus Issue, Global Bifurcations, Chaos, and Hyperchaos: Theory and Applications.
[a)]**Electronic mail:** tinglixing107@gmail.com
[b)]**Author to whom correspondence should be addressed:** pusuluri.krishna@gmail.com
[c)]**Electronic mail:** ashilnikov@gsu.edu

ABSTRACT

Using the technique of Poincaré return maps, we disclose an intricate order of subsequent homoclinic bifurcations near the primary figure-8 connection of the Shilnikov saddle-focus in systems with reflection symmetry. We also reveal admissible shapes of the corresponding bifurcation curves in a parameter space. Their scalability ratio and organization are proven to be universal for such homoclinic bifurcations of higher orders. Two applications with similar dynamics due to the Shilnikov saddle-foci are used to illustrate the theory: a smooth adaptation of the Chua circuit and a 3D normal form.

Published under an exclusive license by AIP Publishing. https://doi.org/10.1063/5.0054776

The bifurcation of the Shilnikov saddle-focus is the key for understanding the origin and structure of deterministic chaos in diverse systems including diverse applications from (astro) physics, neuroscience, and economics. This article is meant to disclose the fine organization of bifurcation unfoldings, including multiple shapes of bifurcation curves in a parameter plane of typical $\mathbb{Z}_2$-symmetric systems. We further develop and showcase the new symbolic approach that lets us disclose a stunning array of homoclinic and heteroclinic bifurcations of the Shilnikov saddle-foci in two representative examples.

I. INTRODUCTION

The aim of this paper is twofold: our first goal, following the pioneering work of Shilnikov on the saddle-focus[1–4] and the two later papers[5,6] on such homoclinic bifurcations, is to examine the structure(s) of bifurcation unfoldings of the primary figure-8 connection in a fully $\mathbb{Z}_2$-symmetric system. The second goal is to illustrate computationally the universality and wealth of such homoclinic bifurcations of the Shilnikov saddle-focus in two representative ordinary differential equation (ODE) systems. The

second part of his paper is partially an extension of our previous works[7–10] on the so-called Lorenz-like systems[11–15] to introduce and demonstrate a new computational approach[16–19] capitalizing on the symbolic description of homoclinic chaos due to Shilnikov saddle-foci in symmetric systems. An important feature of Lorenz-like systems with partial $\mathbb{Z}_2$-symmetry, i.e., $(x, y, z) \leftrightarrow (-x, -y, z)$, is the universality of complex structures in the parameter space, which are due to an abundance of homoclinic bifurcations of the plain (real eigenvalues only) saddle equilibrium state with a pair of 1D unstable separatrices at the origin. Such structures are additionally stirred and interconnected by the characteristic Bykov T-points, corresponding to the heteroclinic connections (of codimension-two) between the saddle and a pair of symmetric saddle-foci. Note that unlike those possessing the full reflection symmetry $(x, y, z) \leftrightarrow (-x, -y, -z)$, a Lorenz-like system cannot accommodate a saddle-focus specifically at the origin of the phase space due to the partial $\mathbb{Z}_2$-symmetry constraint on the 3D phase space (not the case in 4D and higher dimensions though). It is well-known that the occurrence of a single homoclinic orbit of the Shilnikov saddle-focus can give rise to the onset of chaotic dynamics, including countably many nearby periodic orbits in the phase space of such a system. Shilnikov's theory from the 1960s

demonstrated the significance of the organizing role of homoclinic orbits in the hierarchy of deterministic chaos.[20–22]

Let us re-iterate without excessive details what is well-known about the Shilnikov homoclinic saddle focus. The reader is welcome to consult with Shilnikov's original papers[1–3,23–25] and his co-authored textbooks,[26,27] as well as with other relevant papers on the theory[5,6,28–31] by his students and its various extensions[32–36] and diverse applications.[37–47] Figure 1(a) demonstrates the simplest or primary homoclinic orbit to a saddle-focus of the topological (2,1)-type; more details including analytical results will be given in Sec. II. Here, the topological (2,1)-type means that the saddle-focus has a pair of complex conjugate characteristic exponents (small green dots in the inset of Fig. 1) in the left open complex half-plane and one positive real one. The pivotal message of the Shilnikov theorem is that the global structure of the phase space near the homoclinic orbit is solely determined by the local qualities, i.e., characteristic exponents of the saddle-focus per se. To be the Shilnikov saddle-focus, the complex pair is to be the closest to the imaginary axis. Trajectories of a system near such a saddle-focus take a local cross section Π_1^+ transverse to the 2D stable manifold W_{loc}^s and map onto another cross section Π_2 transverse to a 1D unstable separatrix Γ_1. Then, the colored stripes on Π_1^+ will be transformed into a spiral, sometimes called the Shilnikov "snake" with an ordered color pattern on Π_2. Next, the global map takes the spiral and maps it back onto the first

cross section as shown in Fig. 1(b). Depending on the ratio of the local stability to instability at the saddle-focus, there are two generic options—one is when stability [due to the eigenvalue $-\rho$ in Eq. (3)] exceeds instability (due to the positive eigenvalue λ), the overall map is a contraction [Fig. 1(b_1)]; otherwise, it is an expansion [see Fig. 1(b_2)]. Formally speaking, the global dynamics is determined by the sign of the saddle value $\sigma = -\rho + \lambda$ or alternatively on whether the saddle index $\nu = \frac{\rho}{\lambda}$ is greater/less than 1: it is simple when $\sigma < 0$ ($\nu > 1$); otherwise, the dynamics becomes complex if $\sigma > 0$ ($\nu < 1$). In the latter case, the colored (green, blue, and red) stripes in Π_1^+ can be reached from below and crossed, geometrically, by their arched images on the spiral [see Fig. 1(b_2)]. Such crossings are interpreted as the formation of countably many topological Smale horseshoes giving rise to countably many unstable periodic orbits, as well as the onset of complex shift dynamics just near the primary homoclinic orbit in the phase space of the given system. The corresponding 1D return maps are shown in Fig. 1(c). These are basically some "parameterizations" or "projections" of the spirals on coordinate axes. One can see from Fig. 1(c_1) that the contraction map, when shifted up, will produce a single stable fixed point (FP) at the intersection with the 45°-line from the origin in the 1D return map, which corresponds to the saddle-focus in the phase space. On the contrary, the expansion map in Fig. 1(c_2) with characteristic oscillations generates countably many crossings, read FPs, on the 45°-line. When the
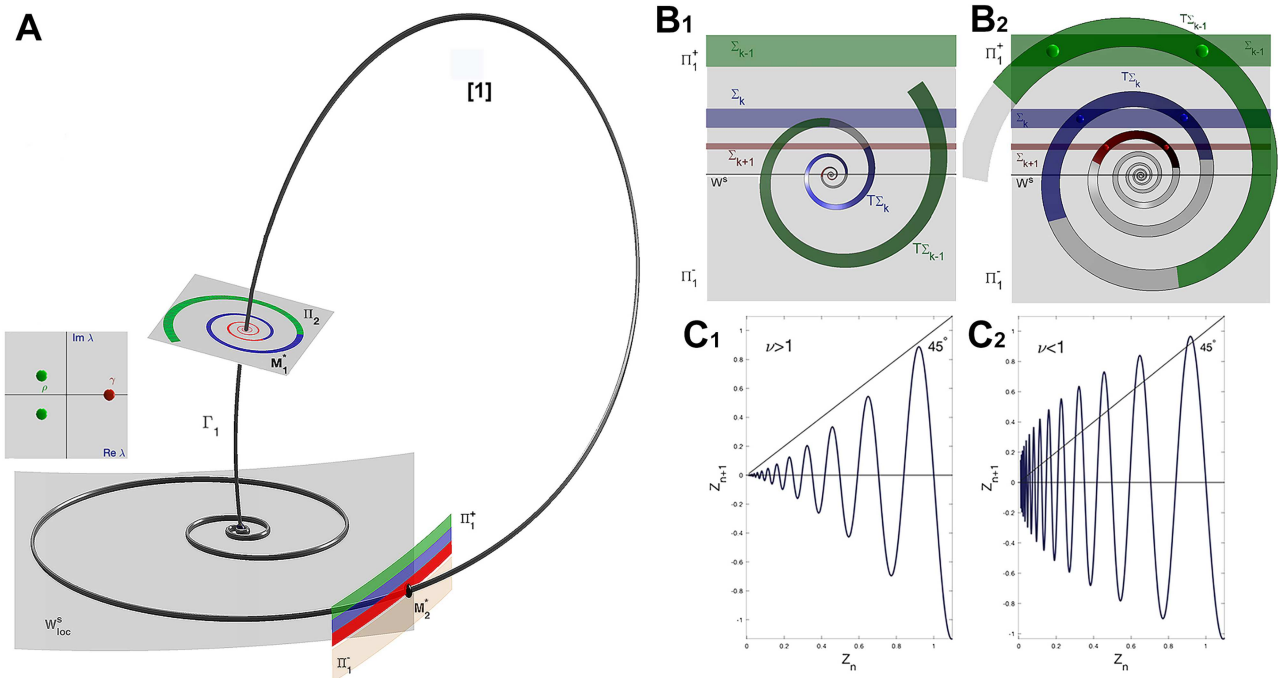

FIG. 1. (a) Primary homoclinic orbit $\bar{\Gamma}_1$ of a saddle-focus of (2,1)-type, i.e., with 2D stable manifold W^s and 1D unstable manifold W^u in $\mathbb{R}^3$. The colored stripes on a local 2D cross section Π_1 transverse to W^s are taken along the trajectories near the equilibrium state to be transformed into a spiral on the local cross section Π_2 transverse to W^u. (b) 2D Poincaré return map $\Pi_2 \rightarrow \Pi_1$ is a contraction in (b_1) with a saddle index $\nu > 1$ [corresponding to a 1D map shown in (c_1)] or an expansion in (b_2) with non-empty intersections $T\Sigma_k \cap \Sigma_k$ giving rise to the onset of countably many Smale horseshoes and saddle POs corresponding to repelling fixed points (FPs) in the 1D map in (c_2) when $\nu < 1$—the so-called Shilnikov condition; from Ref. 23.

homoclinic orbit in Fig. 1(a) splits above/below W_{loc}^s, then the 1D return map, being shifted up/down, nevertheless perseveres most (countably many) of the unstable FPs (corresponding to saddle periodic orbits in the phase space of the given system). Note that some of the "oscillations" of the map graph at $\nu < 1$ will become tangent to the 45°-line to produce new crossings or eliminate them. Such tangencies cause saddle-node bifurcations, soon to be followed by period-doubling ones. This is a reason why the Shilnikov bifurcation in 3D systems is associated with the so-called quasi-chaotic attractors[22] in which hyperbolic subsets (can) coexist with stable periodic orbits emerging through saddle-node bifurcations.[48,49] This is not necessarily the case in higher dominations where tangencies may give rise to saddle–saddle bifurcations; see Refs. 25, 50, and 51.

A representative portrait of deterministic chaos due to three Shilnikov saddle-foci in the phase space (of the smooth Chua model below) is depicted in Fig. 2. This figure also illustrates the concept of a {0, 1}-based binary symbolic description in application to symmetric systems with chaotic dynamics.

As pointed out earlier, this paper includes two parts: a theoretical one followed by computational sections. First, we extend the theory to analytically disclose the structure of local bifurcation unfoldings populated with subsequent homoclinic bifurcations of the Shilnikov saddle-focus, near the primary one (see Figs. 1 and 5) in $\mathbb{Z}_2$-symmetric systems.
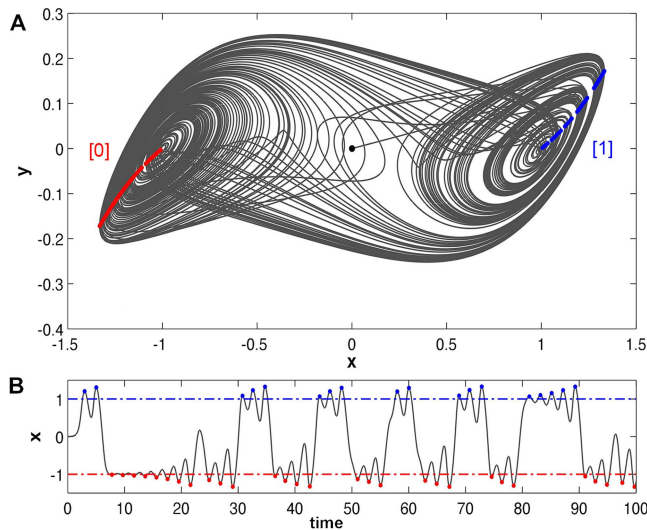

FIG. 2. (a) Homoclinic chaos due to three Shilnikov saddle-foci in the symmetric 3D Chua system (1) at $a = 10.16$ and $b = 14.7$. The right 1D separatrix of the saddle-focus O at the origin (black dot) fills in the double-scroll attractor by making an unpredictable number of turns around and by switching between two other saddle-foci $O_{1,2}(\pm 1, 0, 0)$, separated by our key player—the saddle-focus of the type (2,1) at the origin in the 3D phase space. Its symbolic, binary sequence is generated using a simple rule: [1] or [0] whenever the trajectory turns around O_1 or O_2, respectively, or alternatively, when its x-coordinate reaches a next successive maximum/minimum above/below +1/-1, respectively. See the progression of $x(t)$ in (B).

The second goal of this study is to reveal computationally the self-similar, fine organization of the global bifurcation unfolding of chaos due to the Shilnikov saddle-focus homoclinic bifurcations in two exemplary, $\mathbb{Z}_2$-symmetric systems through detailed visualizations with the aid of a newly proposed computational approach capitalizing on the symbolic description of trajectories on observable strange attractors.

The first example is a smooth approximation of Chua's circuit.[52] The circuit, including two capacitors, two resistors, one inductor, and a nonlinear element, Chua's diode, is described by a 3D system of ODEs, with a single nonlinear term. All of its parameters have specific physical meanings.[53] Originally, the nonlinearity was described using a piece-wise function, which was later replaced with a smooth cubic function in Ref. 54. Both systems were compared in detail in Ref. 53.

The smooth Chua model with a cubic nonlinearity[55,56] is given by

$$\dot{x} = a\left(y + \frac{x}{6} - \frac{x^3}{6}\right), \quad \dot{y} = x - y + z, \quad \dot{z} = -by, \qquad (1)$$

with $a, b > 0$ being bifurcation parameters. The system is reflection or $\mathbb{Z}_2$–symmetric, i.e., invariant under the involution $(x, y, z) \rightarrow (-x, -y, -z)$. It has three equilibrium states: $O(0, 0, 0)$ can be a saddle of the topological type (2,1), i.e., with two 1D unstable separatrices, call them Γ_1 and Γ_2 and a 2D stable manifold W^s, or a saddle-focus of the same topological type, while $O_1(-1, 0, 1)$ and $O_2(1, 0, -1)$ can be stable or saddle-foci of the type (1,2). In the chaotic region of our particular interest in the parameter plane, all three equilibria are saddle-foci. Figure 3 illustrates a bifurcation diagram for the equilibrium states in the cubic Chua model (1); see Refs. 26 and 55 for more details.

The other example employed for the illustration of our symbolic approach to disclose the global organization of homoclinic and heteroclinic bifurcations of the Shilnikov saddle-foci is an asymptotic normal form,[57]

$$\dot{x} = y, \quad \dot{y} = z, \quad \dot{z} = -bz - y + ax(1 - x^2), \qquad (2)$$

with $(a, b) > 0$ being the bifurcation parameters, describing local bifurcation unfolding in systems, near an equilibrium state with a triplet of zero characteristic exponents on a $\mathbb{Z}_2$-symmetric central manifold. Its phase space with three saddle-foci may look similar to that of the cubic Chua model (1). This normal form, as well as some other systems were studied in detail in Refs. 32 and 58–60, which along with the Brussels group,[28,33,34] were the very first works in the West that began studying the Shilnikov saddle-focus and spiral chaos around it. We will refer to Eq. (2) as the cubic Arneodo–Coullet–Spiegel–Tresser (ACST) model after the authors of the series of the publications.

Unlike hyperbolic systems with complex dynamics, the Chua model constantly undergoes abrupt transitions or bifurcations, including homoclinic, saddle-node, and period-doubling, within a parameter region of the existence of the three Shilnikov saddle-foci; see Ref. 5. However, we will not discuss the one-sided chaos due to the two symmetric saddle-foci because its bifurcation structure is essentially the same as observed in the Rössler system; see Refs. 46 and 61. Alternatively, we focus on the symmetric and asymmetric homoclinics generated by the central saddle-focus at the origin, and
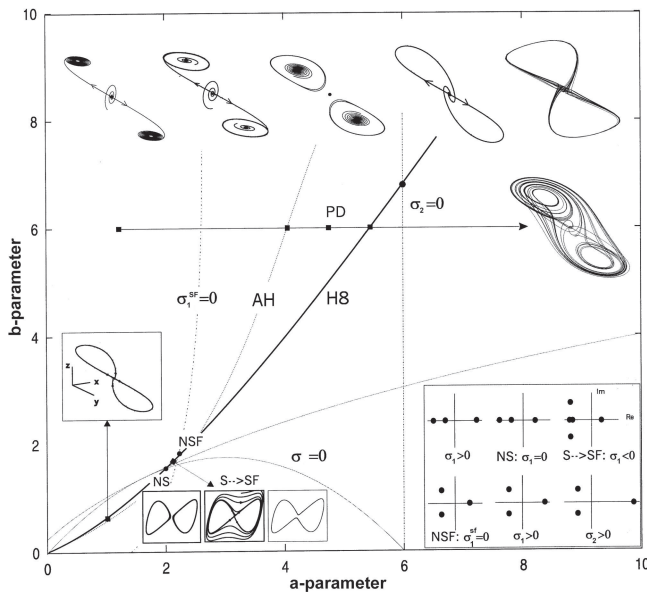
FIG. 3. Bifurcation diagram of the cubic Chua model. Abbreviations AH and H8 stand for, respectively, a supercritical Andronov–Hopf bifurcation of the symmetric equilibria $O_{1,2}$ and a homoclinic figure-8 connection of the saddle/saddle-focus O at the origin, while NS, NSF, and $S \to SF$ stand, respectively, for a neutral (resonant) saddle with a zero saddle value ($\sigma_1 = 0$ or saddle index $\nu = 1$), a saddle-focus with zero saddle value ($\sigma_2^{SF} = 0$ or saddle index $\nu = 1$) and saddle $\Leftrightarrow$ saddle-focus transition with $\sigma_1 < 0$ (see the panel at the right-bottom corner), whereas the crossing point of the vertical line σ_2 with the curve H8 corresponds to the Shilnikov saddle-focus with zero divergence. Along the pathway $b = 6$, first, the 1D unstable separatrices $\Gamma_{1,2}$ of the origin O converge to stable equilibria $O_{1,2}$; next, as the a-parameter is increased, they converge to stable asymmetric periodic orbits (POs) that further lose stability through a first period-doubling (PD) bifurcation in the forthcoming cascade. The pair of the primary saddle POs becomes the figure-8 homoclinic connection of the Shilnikov saddle-focus O, thus giving rise to the onset of homoclinic chaos in the smooth Chua model (1); from Ref. 26.

FIG. 4. Secondary homoclinic orbits of a saddle-focus $(2, 1)$ in the phase space of a $\mathbb{Z}_2$-symmetric system: one-sided double (a) and triple (b) homoclinics encoded symbolically as [11] and [111], respectively. (c) and (d) Figure-8 homoclinic orbits (of Γ_1) with encoded as [10] and [110], respectively. The depicted homoclinic orbits were generated, for the sake of illustration purposes, by solutions of a 4D $\mathbb{Z}_2$-symmetric Shimizu–Morioka type model with the Shilnikov saddle-focus at the origin; see Eq. (C.7.7) on page 924 in Ref. 26.

how their structures are embedded in the parameter space. We use binary symbols [0] and [1] to symbolically encode such homoclinic orbits; see Fig. 4 illustrating the concept. Specifically, [1] is used to describe the passes of the separatrix Γ_1, while [0] is reserved for the other symmetric separatrix Γ_2. For example, double or triple *one-sided* homoclinic orbits are encoded as [11] or [111] or symmetrically as [00] or [000], respectively; see Figs. 4(a) and 4(b). If Γ_1 misses the primary loop and goes underneath the stable manifold W_{loc}^s before it comes back to the saddle-focus as illustrated in Fig. 4(c), then its code is [10]. Figure 4(d) depicts a more complex triple homoclinic orbit encoded as [110].

The paper is organized as follows. In Sec. II, we will present our analytical results on homoclinic bifurcations of the Shilnikov saddle-focus in reflection-symmetric systems. Section III will introduce a symbolic computational tool (see also Refs. 7 and 9) and apply it to the smooth Chua model (1) to compare numerical findings with the theoretical results from Sec. II. Section III will focus on the numerical study of bi-parametric sweeps of the normal form (2), which is followed by conclusions and discussion.
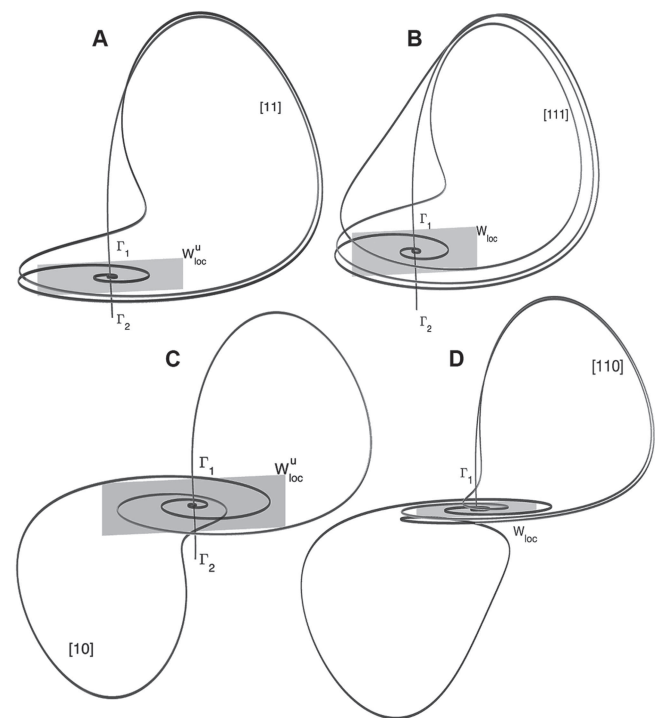
II. ANALYTICAL APPROACH: A HOMOCLINIC BIFURCATION STRUCTURE OF THE SHILNIKOV SADDLE-FOCUS IN SYMMETRIC SYSTEMS

Let us consider the homoclinic Shilnikov saddle-focus of the $(2,1)$-type at the origin O of a 3D system with reflection symmetry. Figure 5 illustrates this where both 1D separatrices $\Gamma_{1,2}$ leave the saddle-focus symmetrically, and after a short excursion, they come back to it along its 2D stable manifold W_O^s. This is called a primary homoclinic figure-8. In what follows, we will consider how small smooth perturbations of a system with such a figure-8 can generate longer subsequent homoclinic orbits of the saddle-focus, under the fulfillment of a single so-called Shilnikov condition.[3] We will also describe how such homoclinic bifurcations are embedded in a parametric plane.

Following Refs. 1 and 23, we consider a saddle-focus $(2,1)$ at the origin in the following $\mathbb{Z}_2$-symmetric system (Note that unlike the linearization assumption requiring the absence of resonant terms, some $\mathbb{C}^{r-1}$-transformations are proposed in Refs. 30 and 31 of coordinates and time, eliminating no-resonant terms in the right-hand side of the original $\mathbb{C}^r$-smooth system, let it be written down in a more suitable form to find its solutions near a saddle equilibrium
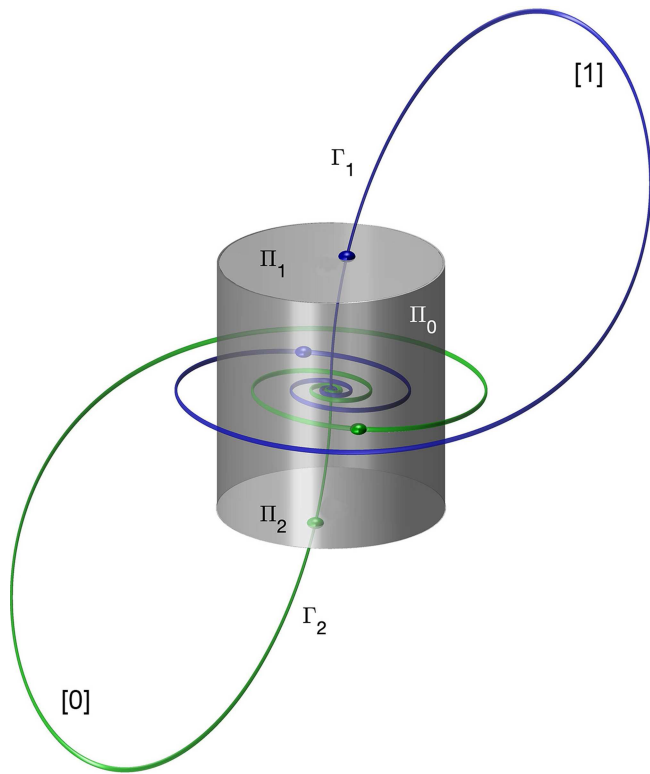
FIG. 5. A pair of the primary homoclinic orbits, symbolically encoded as [1] and [0], of a saddle-focus at the origin in the phase space of a $\mathbb{Z}_2$-symmetric system. The 1D outgoing separatrices Γ_1 and Γ_2 hit outwardly the top Π_1 and bottom Π_2 bases of a cylinder-shaped cross section enclosing the origin and its sidewall Π_0 upon their return to the saddle-focus.

state with stable and unstable invariant manifolds straightened in the affine coordinates; see more in Ref. 26.):

$$
\begin{aligned}
\dot{x} &= -\rho(\mu)x - \omega(\mu)y + F_1(x, y, z, \mu), \\
\dot{y} &= \omega(\mu)x - \rho(\mu)y + F_2(x, y, z, \mu), \qquad (3) \\
\dot{z} &= \lambda(\mu)z + F_3(x, y, z, \mu),
\end{aligned}
$$

where smooth functions F_i, $F_i(\cdot) = -F_i(-(\cdot))$ in the $\mathbb{Z}_2$-symmetric case, vanish at $O(0, 0, 0)$ along with their first derivatives for small μ; the primary homoclinic figure-8 connection occurs at $\mu = 0$. The characteristic exponents of the saddle-focus are given by $-\rho(\mu) \pm i\omega(\mu)$ so that $\rho(\mu)$ and $\omega(\mu) > 0$ and $\lambda(\mu) > 0$. The so-called *saddle index* is given by $\nu(\mu) = \frac{\rho(\mu)}{\lambda(\mu)} < 1$; this is the Shilnikov condition[3] needed for complex dynamics of the finite-shift type to merge in a system with such a saddle-focus. In this normalized system, the z-axis is the linearized unstable manifold W_O^u, and the (x, y)-plane is the linearized stable manifold W_O^s of the saddle-focus at the origin. The solution of the linearized system (3) initiated at a

point (x_0, y_0, z_0) can be written as

$$
\begin{aligned}
x(t) &= e^{-\rho(\mu)t}\left[x_0 \cos(\omega(\mu)t) - y_0 \sin(\omega(\mu)t)\right], \\
y(t) &= e^{-\rho(\mu)t}\left[y_0 \cos(\omega(\mu)t) + x_0 \sin(\omega(\mu)t)\right], \qquad (4) \\
z(t) &= e^{\lambda(\mu)t} z_0.
\end{aligned}
$$

As a transverse cross section, we pick a sufficiently small cylinder (see Fig. 5) enclosing the saddle-focus, to construct a Poincaré return map in cylinder coordinates (r, φ, z), following Ref. 28. It is constructed with a sidewall given by $\Pi_0 : r = R(-R < z < R)$, and top and bottom disks are given by $\Pi_1 : z = R(0 < r < R)$ and $\Pi_2 : z = -R(0 < r < R)$, respectively; here, R is sufficiently small.

For $z_0 > 0$, the local map $T_0 : \Pi_0 \mapsto \Pi_1((\varphi_0, z_0) \mapsto (r, \theta))$ is calculated from Eq. (4), noting that $x_0 = R\cos\varphi_0$, $y_0 = R\sin\varphi_0$, $x(t) = r\cos\theta$, $y(t) = r\sin\theta$, and $z(t) = R$. It is given by

$$
T_0 : \left[
\begin{aligned}
&r = R(z_0/R)^{\nu(\mu)}, \\
&\theta = \varphi_0 + (\omega(\mu)/\lambda(\mu))\ln(R/z_0).
\end{aligned}
\right. \qquad (5)
$$

Similarly, when $z_0 < 0$, the local map $T_0' : \Pi_0 \mapsto \Pi_2((\varphi_0, z_0) \mapsto (r, \theta))$ can be calculated from (4) as

$$
T_0' : \left[
\begin{aligned}
&r = R(-z_0/R)^{\nu(\mu)}, \\
&\theta = \varphi_0 + (\omega(\mu)/\lambda(\mu))\ln(-R/z_0).
\end{aligned}
\right.
$$

The global map $T_1 : \Pi_1 \mapsto \Pi_0$ [which is $(x, y) \mapsto (\varphi_0, z_0)$ or $(r\cos\theta, r\sin\theta) \mapsto (\varphi_0, z_0)$] along the separatrices $\Gamma_{1,2}$, returning to the cylinder-shaped cross section, is approximated by its linear transformation (Likewise, the map obtained by solving the linearized system is a correct approximation of the true local map as nonlinearities due to F_i vanish identically at small (x, y, z).):

$$
T_1 : \left[
\begin{aligned}
\varphi_0 &= a_1\mu + a(\mu)x + b(\mu)y \\
&= a_1\mu + A(\mu)r\cos(\theta + \alpha_1(\mu)) + O(r^2), \\
z_0 &= \mu + c(\mu)x + d(\mu)y \qquad\qquad (6) \\
&= \mu + B(\mu)r\sin(\theta + \alpha_2(\mu)) + O(r^2),
\end{aligned}
\right.
$$

where $A(0)B(0)\cos[\alpha_1(0) - \alpha_2(0)] \neq 0$ for a non-degenerate linear transformation. The map $T_1' : \Pi_2 \mapsto \Pi_0$ can be derived from T_1 using reflection symmetry. For $(x, y) \in \Pi_2$, $T_1'(x, y)$ and $T_1(-x, -y)$ are symmetric with respect to the origin; therefore,

$$
T_1' : \left[
\begin{aligned}
\varphi_0 &= \pi + a_1\mu - A(\mu)r\cos(\theta + \alpha_1(\mu)) + O(r^2), \\
z_0 &= -\mu + B(\mu)r\sin(\theta + \alpha_2(\mu)) + O(r^2).
\end{aligned}
\right.
$$

Hence, when $z_0 > 0$, the complete return map $T = T_1 \circ T_0 : \Pi_0 \mapsto \Pi_0$ is given by

$$T : \begin{bmatrix} \bar{\varphi}_0 = a_1\mu + A(\mu)R(z_0/R)^{\nu(\mu)}\cos\left(\varphi_0 + \dfrac{\omega(\mu)}{\lambda(\mu)}\ln(R/z_0)\right. \\ \left. + \alpha_1(\mu)\right) + O(z_0^{2\nu(\mu)}), \\[2mm] \overline{z_0} = \mu + B(\mu)R(z_0/R)^{\nu(\mu)}\sin\left(\varphi_0 + \dfrac{\omega(\mu)}{\lambda(\mu)}\ln(R/z_0)\right. \\ \left. + \alpha_2(\mu)\right) + O(z_0^{2\nu(\mu)}). \end{bmatrix}$$

For the case $z_0 < 0$, the corresponding return map $T' = T'_1 \circ T'_0 : \Pi_0 \mapsto \Pi_0$ is given by

$$T' : \begin{bmatrix} \tilde{\varphi}_0 = \pi + a_1\mu - A(\mu)R(-z_0/R)^{\nu(\mu)}\cos\left(\varphi_0\right. \\ \left. + \dfrac{\omega(\mu)}{\lambda(\mu)}\ln(-R/z_0) + \alpha_1(\mu)\right) + O(z_0^{2\nu(\mu)}), \\[2mm] \tilde{z}_0 = -\mu + B(\mu)R(-z_0/R)^{\nu(\mu)}\sin\left(\varphi_0\right. \\ \left. + \dfrac{\omega(\mu)}{\lambda(\mu)}\ln(-R/z_0) + \alpha_2(\mu)\right) + O(z_0^{2\nu(\mu)}). \end{bmatrix}$$

Let $A_0 = A(0)$, $B_0 = B(0)$, $\Omega_0 = \omega(0)/\lambda(0)$, $\nu_0 = \nu(0)$, $\phi_1 = -\alpha_1(0) - \Omega_0 \ln R$, and $\phi_2 = -\alpha_2(0) - \Omega_0 \ln R$. Keeping only the dominant terms, these maps can be simplified as follows:

$$T : \begin{bmatrix} \bar{\varphi}_0 = a_1\mu + A_0 R^{1-\nu_0} z_0^{\nu_0}\cos(\Omega_0 \ln z_0 + \phi_1 - \varphi_0) \\ \quad + O(z_0^{2\nu_0}), \\ \bar{z}_0 = \mu - B_0 R^{1-\nu_0} z_0^{\nu_0}\sin(\Omega_0 \ln z_0 + \phi_2 - \varphi_0) \\ \quad + O(z_0^{2\nu_0}) \end{bmatrix} \quad (7)$$

and

$$T' : \begin{bmatrix} \tilde{\varphi}_0 = \pi + a_1\mu - A_0 R^{1-\nu_0}(-z_0)^{\nu_0}\cos(\Omega_0 \ln(-z_0) \\ \quad + \phi_1 - \varphi_0) + O(z_0^{2\nu_0}), \\ \tilde{z}_0 = -\mu - B_0 R^{1-\nu_0}(-z_0)^{\nu_0}\sin(\Omega_0 \ln(-z_0) \\ \quad + \phi_2 - \varphi_0) + O(z_0^{2\nu_0}). \end{bmatrix} \quad (8)$$

A homoclinic orbit that passes l times through the cylinder-wall Π_0 is called an l-loop homoclinic orbit, while shorter ones with two and three passes are called double- and triple-loop homoclinic orbits, respectively. Whenever either 1D separatrix Γ_i hits Π_0 with $z > 0$, we extend its encoding with the symbol 1; otherwise, if $z < 0$, its code is extended with the symbol 0. For example, a homoclinic orbit that passes through Π_0 two times with $z > 0$ is called a one-sided double separatrix [11]-loop/homoclinic orbit [see Fig. 4(a) and 4(b)–4(d) for longer homoclinic orbits and their symbolic codes, respectively]. The μ-parameter is often referred to as a splitting parameter whose positive/negative variations split the primary homoclinic orbit, say $\bar{\Gamma}_1$, upward/downward with respect to the saddle-focus or its stable manifold W^s_{loc}.

Figure 1(c) presents the truncated 1D Poincaré return map $T : z_0 \to \bar{z}_0$

$$\bar{z}_0 = \mu - B_0 R^{1-\nu_0} z_0^{\nu_0}\sin(\Omega_0 \ln z_0 + \phi_2) \quad (9)$$

at $\mu = 0$ and with $z > 0$. The shape of the map is due to the sine-wave function, with its amplitude or envelope bounded by $\pm B_0 R^{1-\nu_0} z_0^{\nu_0}$ $(0 < \nu_0 < 1)$, while the frequency of its zeros increases logarithmically as z approaches 0^+. The return map for $z < 0$ is the mirror reflection of the map (9). Small variations of μ vertically shift the map's graph slightly (Figs. 7 and 8), while z_0-variations squeeze or stretch it horizontally.

Figure 6 demonstrates several 1D return maps for different μ-values. In particular, Fig. 6(a) and $b_{1,2}$ illustrate multiple [11]- and [00]-homoclinic orbits for a fixed value of the saddle index ν_0, while Fig. 6(c) represents terminal triple [111] and [000] orbits (compare with Fig. 4). In these maps, forward iterates of the origin take it back (to O) after two or three steps, respectively. One can infer that such orbits should come in pairs and that the corresponding bifurcation curves must be of a U-shape, with a critical point associated with tangency, like the one in Fig. 6(c). Moreover, an examination of the maps suggests that there are countably many such orbits and bifurcations accumulating to $\mu = 0$. Similarly, Figs. 6(d) and 6(e) show the 1D return maps corresponding to symmetric homoclinic orbits such as [01]/[10] and [110]/[001] that also come in pairs on every oscillation of the map. These conjectures will be proved analytically below.

A. [11]-double homoclinic orbits and bifurcations

Figure 4 illustrates a [11]-double homoclinic orbit where the 1D unstable separatrix Γ_1 slightly misses the saddle-focus above its 2D manifold W^s_{loc} after the first loop. It comes back by intersecting the cross section Π_0 at $(\varphi_0, z_0) = (a_1\mu, \mu)$, where $\mu > 0$. According to the map (7), the next intersection point of Γ_1 with Π_0 is found from these equations

$$\varphi_1 = a_1\mu + A_0 R^{1-\nu_0}\mu^{\nu_0}\cos(\Omega_0 \ln \mu + \phi_1) + O(\mu^{2\nu_0}),$$
$$z_1 = \mu - B_0 R^{1-\nu_0}\mu^{\nu_0}\sin(\Omega_0 \ln \mu + \phi_2) + O(\mu^{2\nu_0}), \quad (10)$$

where the small term $\varphi_0 = a_1\mu$ can be omitted.

The [11]-double homoclinic orbit occurs when $z_1 = 0$; i.e.,

$$\mu + O(\mu^{2\nu_0}) = B_0 R^{1-\nu_0}\mu^{\nu_0}\sin(\Omega_0 \ln \mu + \phi_2), \quad (11)$$

which is equivalent to

$$\mu^{1-\nu_0} + O(\mu^{\nu_0}) = B_0 R^{1-\nu_0}\sin(\Omega_0 \ln \mu + \phi_2). \quad (12)$$

As long as μ is sufficiently small and $\nu_0 < 1$, then we can assume $B_0 R^{1-\nu_0}\sin(\Omega_0 \ln(\mu) + \phi_2) = 0$. The solutions of this equation are $\mu_1^{(n)} = e^{-\frac{2n\pi}{\Omega_0} - \frac{\phi_2}{\Omega_0}}$ and $\mu_2^{(n)} = e^{-\frac{2n\pi}{\Omega_0} \pm \frac{\pi}{\Omega_0} - \frac{\phi_2}{\Omega_0}}$ for sufficiently large n. In this expression, "+" is used for $B_0 > 0$, and "−" for $B_0 < 0$. Without loss of generality, $B_0 > 0$ is assumed. Note that if $z_1 < 0$ for $\mu \in (\mu_1^{(n)}, \mu_2^{(n)})$, then Γ_1 goes underneath W^s_{loc} of the saddle-focus after the second loop, and therefore, no sequential one-sided [11 . . . .] homoclinic orbits or bifurcations can occur when $\mu \in (\mu_1^{(n)}, \mu_2^{(n)})$. This situation is illustrated by the 1D maps presented in Figs. 6(b_1) and 6(b_2), between which the separatrix
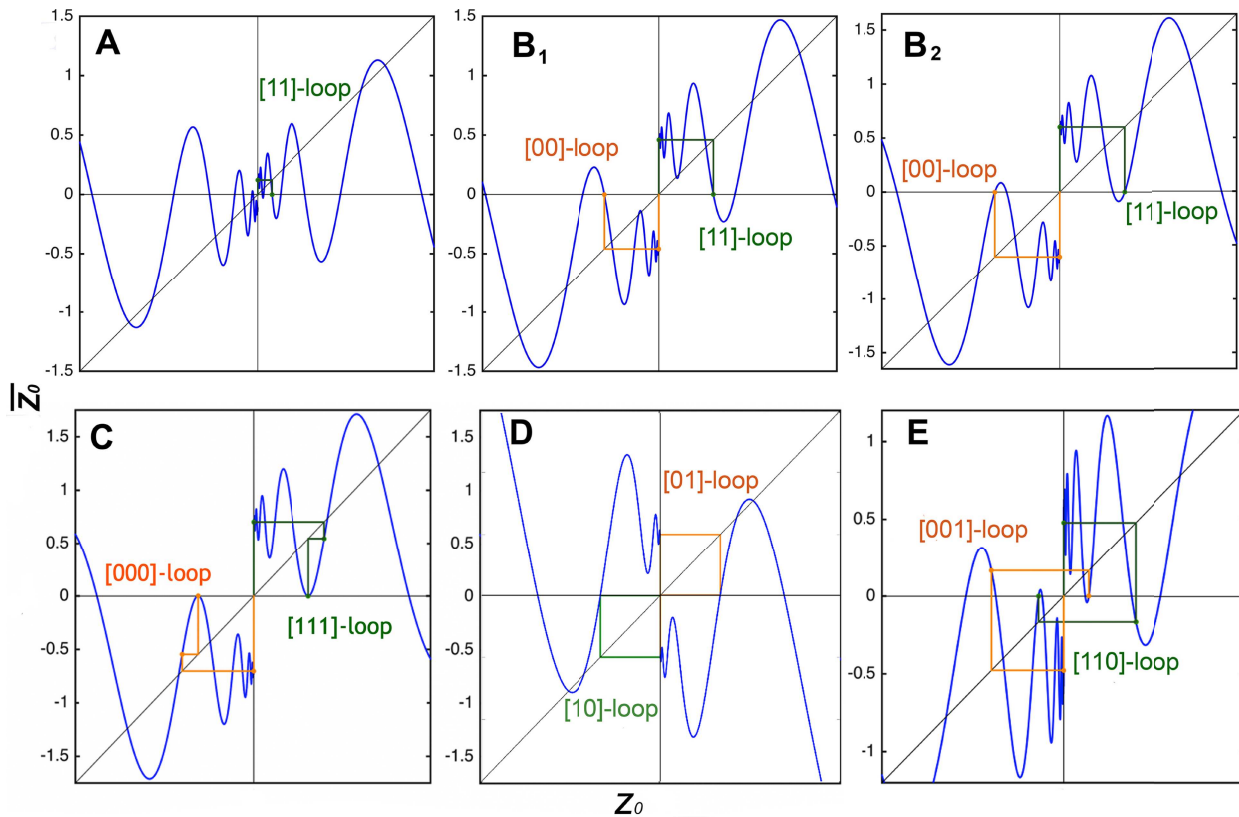
FIG. 6. 1D Poincaré return maps associated with the subsequent homoclinic orbits of the saddle-focus in the phase space shown in Fig. 4: the forward iterates of the origin correspond to the 1D unstable separatrices returning to the saddle-focus. (a) and (b) Multiplicity of symmetric double homoclinic orbits encoded with [11] and [00] is due to countably many zeros in the 1D oscillatory map near such a saddle-focus. (c) Triple homoclinic orbits encoded with [111] and [000], like the homoclinics shown in Fig. 4(b). (d) and (e) Unlike *one-sided* orbits, these 1D maps generate multiplicity of more complex pairs of figure-8 orbits such as [10]/[01] and [110]/[001], similar to those shown in Figs. 4(c) and 4(d), respectively.

falls down below the two zeros of the given U-shaped section of the oscillatory return map.

Figures 7(b) and 8(b) depict the organization of [11]-homoclinic bifurcation curves in the (μ, ν_0)-parameter plane. Vertical ∩-shaped (rounded) bars filled with blue color represent the parameter regions subject to the condition $z_1 < 0$, whereas their borderlines correspond to the [11]-homoclinic bifurcations; i.e., they are the corresponding bifurcation curves of the [11]-orbits. The widths w_n and the distances d_n between any two closest ∩-shaped bars, evaluated as $w_n = \mu_2^{(n)} - \mu_1^{(n)}$ and $d_n = \mu_1^{(n)} - \mu_2^{(n-1)}$, respectively, decrease proportionately as $n \to \infty$ ($\mu \to 0$), as given by the following ratios:

$$\frac{w_{n+1}}{w_n} = \frac{\mu_2^{(n+1)} - \mu_1^{(n+1)}}{\mu_2^{(n)} - \mu_1^{(n)}} = e^{-\frac{2\pi}{\Omega_0}}$$

and

$$\frac{d_{n+1}}{d_n} = \frac{\mu_1^{(n+1)} - \mu_2^{(n)}}{\mu_1^{(n)} - \mu_2^{(n-1)}} = e^{-\frac{2\pi}{\Omega_0}}.$$

Hence, both distance and width shrink exponentially fast as they accumulate to the primary homoclinic bifurcation—the vertical line $\mu = 0$ in the (μ, ν_0)-diagram [see Figs. 7(b) and 8(b)].

When $\nu_0 \to 1$, the term $\mu^{1-\nu_0}$ is no longer negligible but significant in Eq. (12). In this case, solving $\mu^{1-\nu_0} = B_0 R^{1-\nu_0} \sin(\Omega_0 \ln \mu + \phi_2)$ or equivalently $\mu = B_0 R^{1-\nu_0} \mu^{\nu_0} \sin(\Omega_0 \ln \mu + \phi_2)$ gives $z_1 = 0$. These equations can also be interpreted geometrically, see Figs. 7(a) and 8(a), respectively, for the cases $B_0 < 1$ and $B_0 > 1$. Specifically, the sought condition $z_1 = 0$ needed for a [11]-homoclinic orbit to close is fulfilled at all intersections of the "sine" function $y = B_0 R^{1-\nu_0} \mu^{\nu_0} \sin(\Omega_0 \ln \mu + \phi_2)$ and the line $L_0 : y = \mu$. As such, the union of all blue intervals [Figs. 7(a) and 8(a)] gives the range of μ-values for which $z_1 < 0$ for a given constant ν_0. As $\nu_0 \to 1$, the amplitudes/envelopes $C_{1,2} : y = \pm B_0 R^{1-\nu_0} \mu^{\nu_0}$ of the sine function $B_0 R^{1-\nu_0} \mu^{\nu_0} \sin(\Omega_0 \ln \mu + \phi_2)$ flatten and transform into the two lines $L_{1,2}$ given by $y = \pm B_0 \mu$ eventually.

If $B_0 < 1$, the blue μ-intervals start shrinking and vanish after the local maximums of the sine function are lowered below the line L_0; see Fig. 8(a). The closer such a μ-interval is placed to $\mu = 0$, the larger value of ν_0 is needed for the interval to vanish. In the
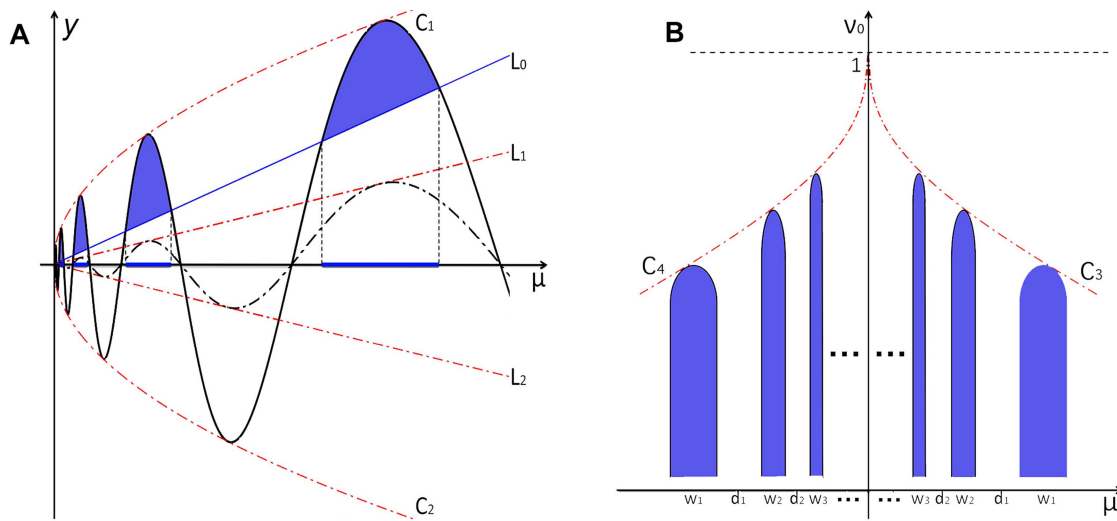
FIG. 7. Panels illustrating the causality and structure of the bifurcation unfolding of the 1D Poincaré return map (9) in the region of $z_1 < 0$ when $B_0 < 1$. (a) Condition $z_1 < 0$ is fulfilled on the graph segments where the sine function is above the line L_0. The union of the projected (blue) intervals yields the range of μ-values resulting in $z_1 < 0$. The interval end points correspond to the formation of the double [11]- and [00]-homoclinic orbits. As $\nu_0 \to 1$, the amplitude $C_{1,2}$ of the sine function flattens to two lines, $L_{1,2}$, causing the blue intervals to vanish. (b) Sketch of the (μ, ν_0)-plane with the colored regions, also known as blue $\cap$-bars, in which $z_1 < 0$. The outlines of the blue $\cap$-bars on the $\mu > 0$-side correspond to the double [11]/[00] homoclinic orbits. The outlines of the blue $\cap$-bars on the $\mu < 0$ side correspond to the double [10]/[01]-orbits. The blue bars are bounded from above by the $C_{3,4}$-curves; w_j and d_j stand for the widths and the distances between the bars, respectively.

(μ, ν_0)-parameter diagram, the corresponding region looks like a vertical $\sqcap$-bar with the tipping point cut out when $\mu = B_0 R^{1-\nu_0} \mu^{\nu_0}$ or $\nu_0 = 1 - \frac{\ln B_0}{\ln \mu - \ln R}$. This equality is held on the red dash C_3-curve in the (μ, ν_0)-parameter diagram in Fig. 7(b). This (cusp-shaped) C_3-curve approaches the level $\nu_0 = 1$ from below as $\mu \to 0$. The vertical bars that terminate before reaching the horizontal line $\nu_0 = 1$ all have the $\cap$-shape.

In the case $B_0 > 1$, the bars and the intervals between them become narrower as $\nu_0 \to 1$, but they persist [Fig. 8(a)]. In the (μ, ν_0)-parameter diagram, the condition $z_1 < 0$ is held in the union of all blue $\sqcap$-shaped bars below the level $\nu_0 = 1$; see Fig. 8(b).

B. [10]-double homoclinic bifurcations

A typical [10]-double homoclinic orbit is illustrated in Fig. 4(c). The corresponding 1D return map is shown in Fig. 6(d). By construction, after the separatrix Γ_1 runs a single [1]-loop on its way back to the saddle-focus, it goes underneath its stable manifold W_{loc}^s and hits the cross section Π_0 at $(\varphi_0, z_0) = (a_1\mu, \mu)$ with $\mu < 0$, and then it completes the second [0]-loop heading toward the equilibrium state. It hits Π_0 for the second time at some point (φ_1, z_1), which can be found by the return map as follows:

$$\varphi_1 = \pi + a_1\mu - A_0 R^{1-\nu_0}(-\mu)^{\nu_0} \cos(\Omega_0 \ln(-\mu) + \phi_1)$$
$$+ O((-\mu)^{2\nu_0}),$$
$$(13)$$
$$z_1 = -\mu - B_0 R^{1-\nu_0}(-\mu)^{\nu_0} \sin(\Omega_0 \ln(-\mu) + \phi_2)$$
$$+ O((-\mu)^{2\nu_0}).$$

The condition $z_1 = 0$, i.e.,

$$-\mu + O((-\mu)^{2\nu_0}) = B_0 R^{1-\nu_0}(-\mu)^{\nu_0} \sin(\Omega_0 \ln(-\mu) + \phi_2),$$

corresponds to the occurrence of a [10]-double homoclinic orbit. One can observe that this condition is similar to the case of [11]-homoclinic orbits where μ is replaced with $-\mu$. Therefore, the structure of the bifurcation unfolding for [10]-homoclinic orbits is flip-symmetric ($\mu \to -\mu$) to the bifurcation diagram for the [11]/[00]-homoclinics; see Figs. 7(b) and 8(b).

Now, we arrive at the following theorem for double homoclinic orbits.

Theorem 1. *Let a reflection-symmetric system have a pair of primary homoclinics to the Shilnikov [$\nu(\mu) < 1$] saddle-focus at $\mu = 0$. Then, double homoclinics occur at values*

$$|\mu| = B_0 R^{1-\nu_0} |\mu|^{\nu_0} \sin(\Omega_0 \ln|\mu| + \phi_2),$$

where $B_0, R > 0$ are constants. If $B_0 < 1$, then the (μ, ν_0)-parameter diagram includes countably many $\cap$-shaped bifurcation curves corresponding to double homoclinics that are topped up by the curve, $\nu_0 = 1 - \frac{\ln B_0}{\ln|\mu| - \ln R}$, converging to 1 as $\mu \to 0$. All such double-bifurcations accumulate to the primary one from both sides with a scalability ratio $e^{-\frac{2\pi}{\Omega_0}}$ for both the width and the distance between the bifurcation curves.

C. [111]-triple homoclinic orbits and bifurcations

A typical [111]-triple homoclinic orbit of the saddle-focus in the phase space is illustrated in Fig. 4(b). Recall that such orbits, [111...], are all one-sided, so to say. The corresponding 1D return
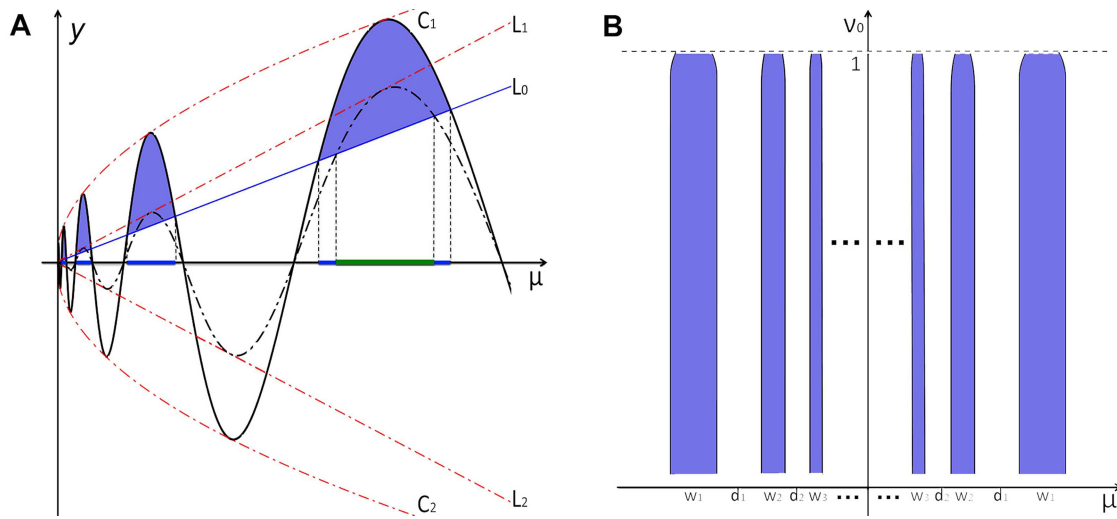
FIG. 8. Panels illustrating the causality and structure of the bifurcation unfolding of the 1D Poincaré return map (9) in the region of $z_1 < 0$ when $B_0 > 1$. (a) $z_1 < 0$ is fulfilled on the graph segments where the sine function is above the line L_0. Blue intervals on the μ-axis are where $z_1 < 0$. The interval end point is the bifurcation μ-values corresponding to one-sided [11]/[00] homoclinic orbits. As $\nu \to 1$, the envelopes $C_{1,2}$ of the sine function flatten to the $L_{1,2}$-lines, thereby making the blue intervals shorten to the green intervals. (b) The plot sketches the regions in the (μ, ν_0)-parameter plane—blue Π-bars—where $z_1 < 0$. The outlines of the blue Π-bars on the $\mu > 0$-side are the bifurcation curves of the double [11]/[00]-orbits. The outlines of the blue Π-bars on the $\mu < 0$-side correspond to [10]/[10] double homoclinic orbits; here, w_j and d_j stand for the widths and distances between the bars, respectively.

map for a critical [111]-orbit is shown in Fig. 6(c) where the origin is taken back to zero, here single or critical, meaning that such a homoclinic orbit may no longer occur for the given map, should the splitting parameter μ be increased. This tangency at zero in the map corresponds to the turning point of a $\cap$-shaped homoclinic bifurcation curve, like ones shown in Fig. 7(b).

Therefore, let the unstable separatrix Γ_1 make three such loops prior to its returning to the saddle-focus along its W_{loc}^s. Then, the corresponding truncated map, accounting for the dominant terms only, is given by

$$z_1 = \mu - B_0 R^{1-\nu_0} \mu^{\nu_0} \sin(\Omega_0 \ln \mu + \phi_2) + O(\mu^{2\nu_0}),$$
$$z_2 = \mu - B_0 R^{1-\nu_0} z_1^{\nu_0} \sin(\Omega_0 \ln z_1 + \phi_2) + O(z_1^{2\nu_0}) \quad (14)$$

(equations for φ-variables are omitted). To find the bifurcation curves corresponding to [111]-triple homoclinics, one must first identify the μ-range where $z_2 < 0$.

The first part in Eq. (14) implies that $z_1 \sim \mu^{\nu_0}$, and therefore, z_1 is small when μ is small. The second equation in (14) can be further reduced to $\sin(\Omega_0 \ln z_1 + \phi_2) = 0$, assuming that μ is small enough. Its solutions are $z_1 = e^{-\frac{2m\pi}{\Omega_0} - \frac{\phi_2}{\Omega_0}}$ or $e^{-\frac{2m\pi}{\Omega_0} + \frac{\pi}{\Omega_0} - \frac{\phi_2}{\Omega_0}}$; here, $m \in \mathbb{Z}$ is sufficiently large. Denote by I_m all intervals of z_1 for such $z_2 < 0$. It can be deduced from the mth period of the sine function that the sought intervals are given by

$$I_m \approx (e^{-\frac{2m\pi}{\Omega_0} - \frac{\phi_2}{\Omega_0}}, e^{-\frac{2m\pi}{\Omega_0} + \frac{\pi}{\Omega_0} - \frac{\phi_2}{\Omega_0}}),$$

with $m \in \mathbb{N}$ being sufficiently large and μ is assumed to be small. Figure 9 illustrates such an interval I_m for some small fixed μ: it is highlighted in green on the z_1-axis within which the mth period of

the sine function, $y = B_0 R^{1-\nu_0} z_1^{\nu_0} \sin(\Omega_0 \ln z_1 + \phi_2)$, is greater than the given μ. Assume that D_m is a local maximum on the mth period of the sine function whose graph is a dashed-line in Fig. 9(b). If $D_m < \mu$, then any such interval I_m shrinks and collapses as $\nu_0 \to 1$. If $D_m > \mu$, in contrast, then I_m narrows down to some (orange) interval that persists in the limit $\nu_0 \to 1$; see Fig. 9(b).

Let us first discuss the case $B_0 < 1$. The first equation (14) can be written as follows:

$$\mu - z_1 = B_0 R^{1-\nu_0} z_1^{\nu_0} \sin(\Omega_0 \ln z_1 + \phi_2) + O(z_1^{2\nu_0}).$$

One can observe that the right-hand side of the equation above is the sine function, like the one shown in Fig. 10(a). Its sections above L_0, which are filled in blue, are the same ones shown in Fig. 7(a), and the boundaries of the blue $\cap$-shape bars in Fig. 10(b) are the [11]-homoclinic bifurcation curves [Fig. 7(b)], which are elaborated on in Sec. II A. Let us examine [111]-homoclinic bifurcations occurring only on one period of the sine function $y = B_0 R^{1-\nu_0} \mu^{\nu_0} \sin(\Omega_0 \ln \mu + \phi_2)$. The chosen period is labeled by end points, A and B, in Fig. 10(a). Consider the nth period given by $\mu \in (e^{-\frac{2n\pi}{\Omega_0} - \frac{\pi}{\Omega_0} - \frac{\phi_2}{\Omega_0}}, e^{-\frac{2n\pi}{\Omega_0} + \frac{\pi}{\Omega_0} - \frac{\phi_2}{\Omega_0}})$. Assume that the function has a local minimum m_n at $\mu_{\min}$ and a local maximum M_n at $\mu_{\max}$. After the bent envelops $C_{1,2}$ are rectified and become the straight lines $L_{1,2}$ at $\nu_0 = 1$, the new local minimum and maximum on the given period are denoted by m'_n and M'_n. Consider [111]-homoclinic bifurcations occurring between two blue bars, a_n and a_{n+1} (corresponding to the occurrence of two consecutive [11]-orbits on the same or similar interval) in the bifurcation diagram in Fig. 10(b).

Recall that $z_2 < 0$ when $z_1 \in I_m$, with $m \in \mathbb{N}$ being sufficiently large. By construction, $y = \mu - I_m$ represents a strip bounded by
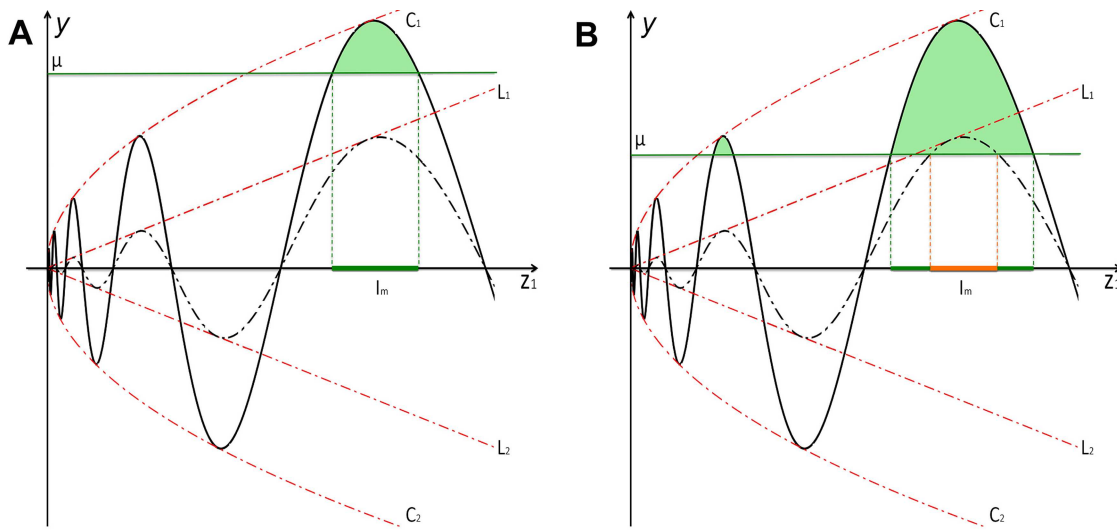
FIG. 9. The graph (solid line) of the sine function $y = B_0 R^{1-\nu_0} z_1^{\nu_0} \sin(\Omega_0 \ln z_1 + \phi_2)$ bounded by the $C_{1,2}$-curves/envelopes. Its section above the horizontal line $y = \mu$ is painted green. The dashed graph is given by the sine function $y = B_0 z_1^{\nu_0} \sin(\Omega_0 \ln z_1 + \phi_2)$ bounded by the $L_{1,2}$-lines. The dashed graph is completely below the line $y = \mu$ in (a), whereas its crossing with the line $y = \mu$ occurs on an orange interval nested within the green interval I_m on the z_1-axis in (b).

two lines nearly parallel for large enough $m \in \mathbb{N}$; see Fig. 10; actually, any two successive lines are no longer parallel if we take into account smaller terms that were neglected earlier. Therefore, the range of μ-values corresponding to $z_2 < 0$ is a union of all the interception intervals of (colored) strips $y = \mu - I_m$, with the curve $y = B_0 R^{1-\nu_0} \mu^{\nu_0} \sin(\Omega_0 \ln \mu + \phi_2)$ projected on the μ-axis. All such strips line up under and accumulate from below to L_0 as m increases. They become narrower while approaching L_0 so that $\frac{|I_{m+1}|}{|I_m|} = e^{-\frac{2\pi}{\Omega_0}}$. Six such colored strips labeled by $S_1, \ldots, S_6$ are sampled in Fig. 10(a) corresponding to multiple distinct [111]-triple orbits and their homoclinic bifurcation curves in the (μ, ν_0)-parameter plane [Fig. 10(b)].

Let the purple strip S_1 at the bottom be the very first one that intercepts the oscillatory graph of the sine function $y = B_0 R^{1-\nu_0} \mu^{\nu_0} \sin(\Omega_0 \ln \mu + \phi_2)$. The projection of this overlap onto the μ-axis, say p_1, is the μ-interval where $z_2 < 0$ for a given constant ν_0. It is located in between two blue intervals, on which the sine function is greater than L_0 [Fig. 10(a)]. In the limit $\nu_0 \to 1$, the bent envelopes $C_{1,2}$ straighten up and become the $L_{1,2}$-lines, which makes the given p_1-interval collapse and vanish. The corresponding image of p_1 is the purple $\cap$-shaped solid bar, say b_{n1}, located in the middle of the two blue $\cap$-shaped bars, a_n and a_{n+1} (corresponding to the condition $z_1 < 0$) in the (μ, ν_0)-parameter plane in Fig. 10(b). In the case of S_2 or S_6, we have the following inequalities $m_n < (\mu - I_m)|_{\mu=\mu_{\min}} < m'_n$ or $M'_n < (\mu - I_m)|_{\mu=\mu_{\max}}$, respectively; i.e., the stripes are bounded by the old and new local minima and maxima on the nth period of the sine function. Figure 10(b) gives an interpretation of these inequalities in the (μ, ν_0)-bifurcation diagram: the corresponding (reddish) region, say b_{n2}, is formed through a merger of two bending vertical bars forming a bridge- or arch-like

connection atop the $\cap$-shaped one b_{n1}; the same is true for the green bending bridges, say b_{n2} and b_{n6}^1 due to the S_6-strip, which are placed on top of the blue bars, a_n and a_{n+1}. The geometric explanation of such a $\cap$-shape is the same: the graph of the sine function no longer crosses S_2 or S_6 as ν_0 is increased or decreased beyond some thresholds corresponding to critical tangencies with these stripes. Clearly, there can be more such bridge-shaped regions in the bifurcation diagram if there are more such strips fitting these conditions.

In addition, a top strip like S_6 can give rise to extra narrow (green) $\cap$-bars located inside every bridge (such as b_{n6} and b_{n6}^1) in Fig. 10(b) provided that it is (i) close to L_0 and (ii) is narrow enough to shrink and vanish before the corresponding two bending bars merge, forming a bridge-like object in the bifurcation diagram in the limit $\nu_0 \to 1$. Otherwise, if the following inequalities $m'_n < (\mu - I_m)|_{\mu=\mu_{\min}}$ and $(\mu - I_m)|_{\mu=\mu_{\max}} < M'_n$ are fulfilled, say for the S_4-strip in Fig. 10(a), then no bridge- or arch-shaped region will be formed through a merger of two bending bars. Alternatively, the corresponding (yellow) structure will look like either a Π-bar (b_{n4}^1) or a $\cap$-bar (b_{n4}^2 to the right from b_{n4}^1) in the (μ, ν_0)-parameter plane in Fig. 10(b). The shape of such bars, Π- or $\cap$-like, is determined by whether the width of the strip or, equivalently, the width of the I_m-interval remains small but finite as in Fig. 9(b) or it collapses as depicted in Fig. 5(a) in the limit $\nu \to 1$. Since a narrower strip is likely to vanish, therefore, the yellow $\cap$-bar resides closer to the blue [11]-orbit bars. If m'_n or M'_n happens to be inside the given strip, like S_3 or S_5, then two of its sections intercepting the graph of the sine function will merge after the minimum or maximum of the sine function moves inside S_3 and S_5, with changes in μ. Meanwhile, both S_3 and S_5 keep narrowing as $\nu_0 \to 1$. Therefore, the extreme (min/max) points can slip away from overlapping with
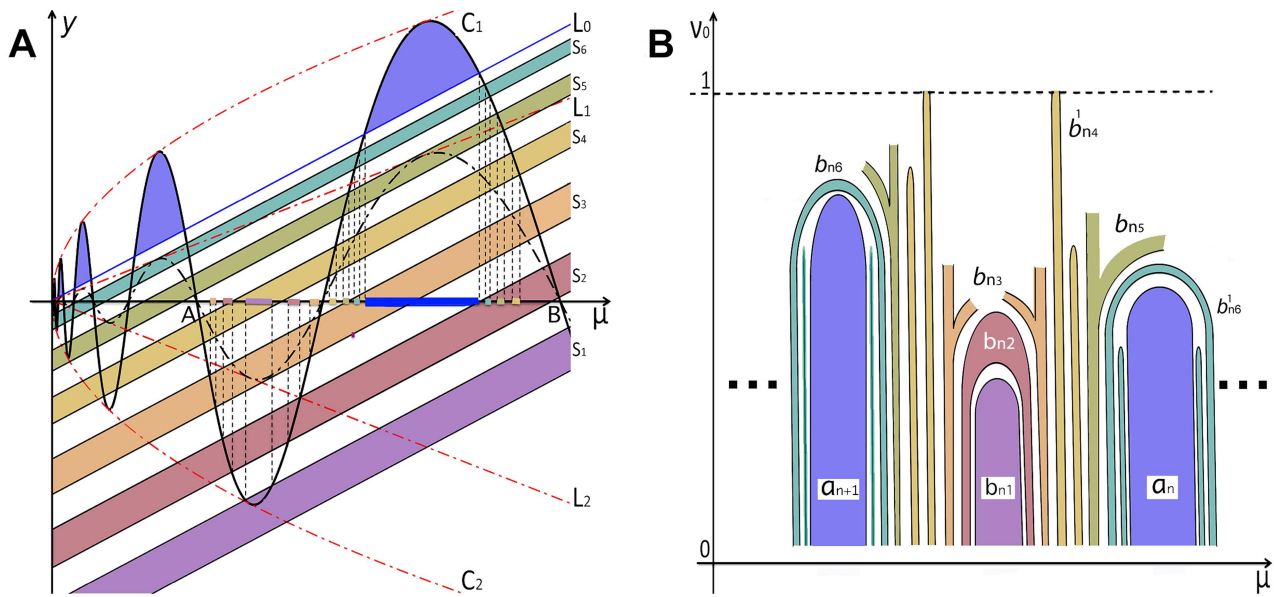
FIG. 10. The case $B_0 < 1$. (a) The solid graph of the sine function $y = B_0 R^{1-v_0} \mu^{v_0} \sin(\Omega_0 \ln \mu + \phi_2)$ bounded by the curves $C_{1,2} : y = \pm B_0 R^{1-v_0} \mu^{v_0}$. The dashed graph of the sine function $y = B_0 \mu \sin(\Omega_0 \ln \mu + \phi_2)$ bounded by the lines $L_{1,2} : y = \pm B_0 \mu$. The interceptions of the solid color strips $S_1 - S_6$, parallel to the line $L_0 : y = \mu$, and the sine function are projected to the μ-axis. The closer a strip is to L_0, the narrower it becomes. (b) (μ, v_0)-parameter plane sketching a bifurcation unfolding including ∩-bars [color matching panel (a)] such as a_n and a_{n+1} (in blue) outlining the double [11]/[00] homoclinic orbits and b_{nj} for triple [111]-orbits. Around each blue bar, there are a pair of narrow ∩-bars and a bridge due to the strip S_6 in (a). Besides, shown are a few Y-shaped bifurcation objects due to intersections of the sine function with the strips S_3 and S_5 and a pair of yellow ∩-bars and a pair of Π-bars generated by strip S_4, as well as a reddish bridge due to the crossing with S_2. Shown in the middle is a purple ∩-bar b_{n1}, which is the widest domain for triple homoclinics orbits; other such regions fit narrow in the parameter space.

S_3 or S_5, which result in the corresponding bridge-like region decoupling into two "Y"-shaped objects. These are depicted in Fig. 10(b) as yellow pair-wise bars, like b_{n3} due to S_3, atop b_{n2}, and greenish Y-shaped bars like b_{n5} due to S_5. Both branches remain left-open as they may end up differently with parameter variations. Either branch of a Y-shaped bar can bridge with the symmetric one or they both terminate prior to merging into one. A bar like b_{n3} can also morph into the shape of the bar next to it, of the Π- or ∩-shape. Thus, the Y-shape can be viewed as a transition between the bridge and the ∩-bar. It is easy to argue that there can be a single Y-shaped region or none generated by each strip like S_3 or S_5. Let $b_{n1}, \ldots, b_{n6}$ be referred to as [111]-triple homoclinic zones. One or more of such zones would be absent in the bifurcation diagram sketched in Fig. 10(b) if there were no strips passing throughout the corresponding position in Fig. 10(a) and so forth. For example, the b_{n1}-zone may no longer be present if the strip S_1 were positioned to go through the sine function in the way the strip S_2 does. Another example is S_4: if the relative positions of μ and the z_1 sine function for all S_4 strips were such as shown in Fig. 9(b), then the b_{n4}^2-bars would not be spotlighted in Fig. 10(b).

Note that a [111]-zone in Fig. 10(b) becomes the thicker, the further it is away from the closest blue ∩-bars a_n and a_{n+1}. Therefore, b_{n1}, if it exits, is significantly larger than others because the strip S_1 intercepts the graph of the sine function at its flattest section near the critical point. Actually, by computing the derivative of the sine

function $y = B_0 R^{1-v_0} \mu^{v_0} \sin(\Omega_0 \ln \mu + \phi_2)$, we obtain

$$\frac{dy}{d\mu} = \frac{N_2}{\mu^{1-v_0}} \sin(\Omega_0 \ln \mu + \phi_2 + \theta_0), \qquad (15)$$

where $N_2 = B_0 R^{1-v_0} \sqrt{v_0^2 + \Omega_0^2}$ and $\cos\theta_0 = v_0 / \sqrt{v_0^2 + \Omega_0^2}$. For a fixed $v_0 < 1$, $\frac{dy}{d\mu}$ is large because μ is small. Therefore, the graph of the sine function looks as if it is made of vertical (and horizontally dense) lines except for small neighborhoods of critical points of $y = B_0 R^{1-v_0} \mu^{v_0} \sin(\Omega_0 \ln \mu + \phi_2)$. The overlapping of S_1 with the sine function is one such neighborhood. Therefore, the width of b_{n1} is to be significantly larger compared to those of other [111]-zones.

On the other hand, the width of a [111]-zone increases with increasing μ because $\frac{dy}{d\mu}$ decreases in Eq. (15); see such zones on the right from b_{n1} sketched in Fig. 10(b), which should look slightly wider than the symmetric zones on the left from b_{n1}. We conclude by remarking the very middle zone—the purple bar b_{n1} being furthest from a_n and a_{n+1} is sketched to be of the largest width. Note that in computational sweeps, such an associated purple bar or a reddish bridge if the former one does not exist can be the only visible or recognizable [111]-zone, as all others might be too narrow to detect. We reiterate that the borderlines of such zones in the (μ, v_0)-parameter plane are the bifurcation curves corresponding to [111]-triple homoclinic orbits.
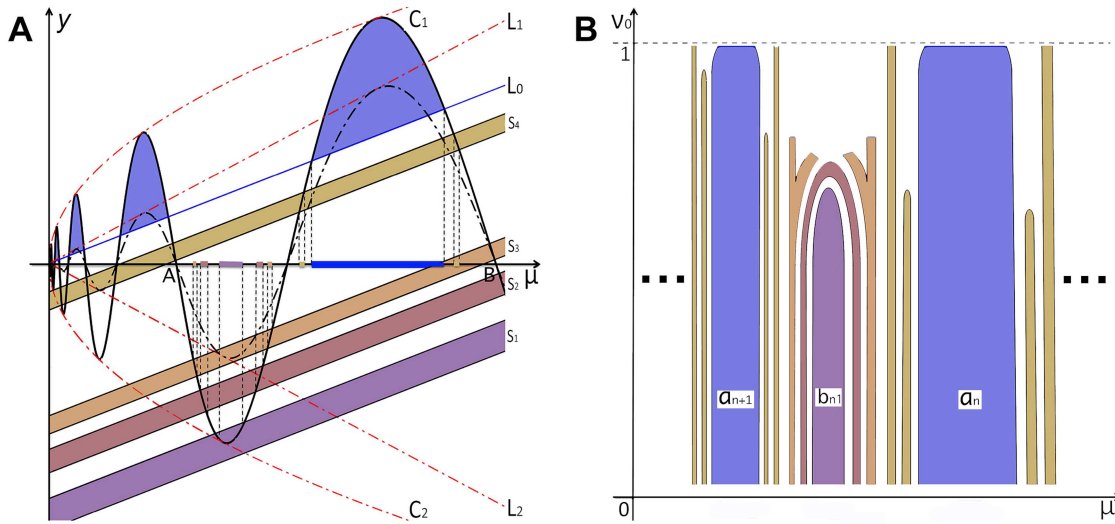
FIG. 11. $B_0 > 1$. (a) The sine function is $y = B_0 R^{1-v_0} \mu^{v_0} \sin(\Omega_0 \ln \mu + \phi_2)$ bounded by $C_{1,2} : y = \pm B_0 R^{1-v_0} \mu^{v_0}$. The dashed sine function is bounded by $L_{1,2}$: $y = \pm B_0 \mu$. The interceptions of the strips $S_1 - S_4$ and the sine function are projected onto the μ-axis. The strips are parallel to the line $L_0 : y = \mu$. The closer a strip is to L_0, the narrower it is. (b) Two blue (1, 1) double-loop bars, a_n and a_{n+1}, are drawn on the (μ, v_0)-plane. The (1, 1, 1) triple-loop bars fit in between and match the color of the strips in the plot (a) that they are derived from. We describe it in the order from the close region of a blue bar to its furthest. Close to the blue bar, there are a pair of yellow ∩-bars and a pair of yellow Π-bars that are derived from the strip S_4. Then, there is a pair of "Y" shapes that are derived from S_3. Then, there is a reddish bridge that is derived from S_2. In the middle of the two blue bars, there is a purple ∩-bar b_{n1} that is the widest triple-loop piece. The closer to the blue bar, the narrower the triple-loop piece is. Taking b_{n1} as the center, the left pieces are slightly narrower than the right pieces.

Figure 11 is meant to aid with describing the region where $z_2 < 0$ and hence with detecting [111]-homoclinic bifurcations when $B_0 > 1$. Unlike its predecessor, it does include the strips S_5 and S_6 and the corresponding bifurcation zones. One can see that the bifurcation diagram in Fig. 11(b), still featuring the bridges atop b_n and a_{n+1} along with transitional Y-shaped bars, is similar to that in the case $B_0 < 1$.

D. [100]-triple homoclinic orbits and bifurcations

A similar, [110]-triple homoclinic orbit is pictured in Fig. 4(d). Unlike it, the unstable separatrix Γ_1 makes one loop above and two loops underneath the stable manifold W^s before it returns to the saddle-focus to complete a [100]-homoclinic orbit. The corresponding z-return map with the dominant terms only is given by

$$z_1 = -\mu - B_0 R^{1-v_0}(-\mu)^{v_0} \sin(\Omega_0 \ln(-\mu) + \phi_2) + O((-\mu)^{2v_0}),$$
$$\tag{16}$$
$$z_2 = -\mu + B_0 R^{1-v_0}(-z_1)^{v_0} \sin(\Omega_0 \ln(-z_1) + \phi_2) + O((-z_1)^{2v_0}),$$

where $\mu < 0$. As before, we seek the range of μ-values such that $z_2 < 0$ for a fixed v_0. By varying v_0, we identify the regions in the (μ, v_0)-bifurcation diagram corresponding to the condition $z_2 < 0$. The boundaries of these regions are the bifurcation curves associated with [100]-homoclinic orbits.

Equation (16) implies that $-z_1 \sim (-\mu)^{v_0}$; hence, z_1 is small when $-\mu$ is small. Omitting the small term $-\mu$, the second equation in (16) can be further simplified: $\sin(\Omega_0 \ln(-z_1) + \phi_2) = 0$; i.e., $-z_1 = e^{-\frac{2m\pi}{\Omega_0} - \frac{\phi_2}{\Omega_0}}$ or $e^{-\frac{2m\pi}{\Omega_0} - \frac{\phi_2}{\Omega_0} + \frac{\pi}{\Omega_0}}$ with $m \in \mathbb{Z}$ large enough. The interval I_m of $-z_1$-values such that $z_2 < 0$, derived from the mth period of the sine function, can be estimated as $\left(e^{-\frac{2m\pi}{\Omega_0} - \frac{\phi_2}{\Omega_0}}, e^{-\frac{2m\pi}{\Omega_0} - \frac{\phi_2}{\Omega_0} + \frac{\pi}{\Omega_0}} \right)$. As was discussed previously, I_m is actually μ-related if we consider some negligible small μ-term. The length of I_m can either decrease to zero [Fig. 9(a)] or decrease to a small fixed number [Fig. 9(b)] as $v_0 \to 1$.

Let us first elaborate on the case $B_0 > 1$. The first equation of the system (16) can be written as

$$-\mu - z_1 = B_0 R^{1-v_0}(-\mu)^{v_0} \sin(\Omega_0 \ln(-\mu) + \phi_2) + O((-\mu)^{2v_0}).$$

The right-hand side is the sine function of $-\mu$, whose graph is depicted in Fig. 12(a), with $-\mu$ being on the x axis. Its graph sections, painted in blue, above $L_0 : y = -\mu$ let the μ-intervals be identified within which [10]-homoclinic bifurcations occur, as discussed previously. Recall that $z_2 < 0$ when $-z_1 \in I_m$ (here, $m \in \mathbb{Z}$ is to be large enough), and therefore, the range of μ-values such that $z_2 < 0$ is the projection of the interceptions of the line $y = (-\mu) + I_m$ with the graph of $y = B_0 R^{1-v_0}(-\mu)^{v_0} \sin(\Omega_0 \ln(-\mu) + \phi_2)$ onto the $(-\mu)$-axis. Then, for each m, the quantity $y = (-\mu) + I_m$ is geometrically interpreted as a strip that is parallel to and above the line L_0. The domain of $-\mu$ such that $z_2 < 0$ is the projection of the overlaps of all such strips and the graph of the sine function
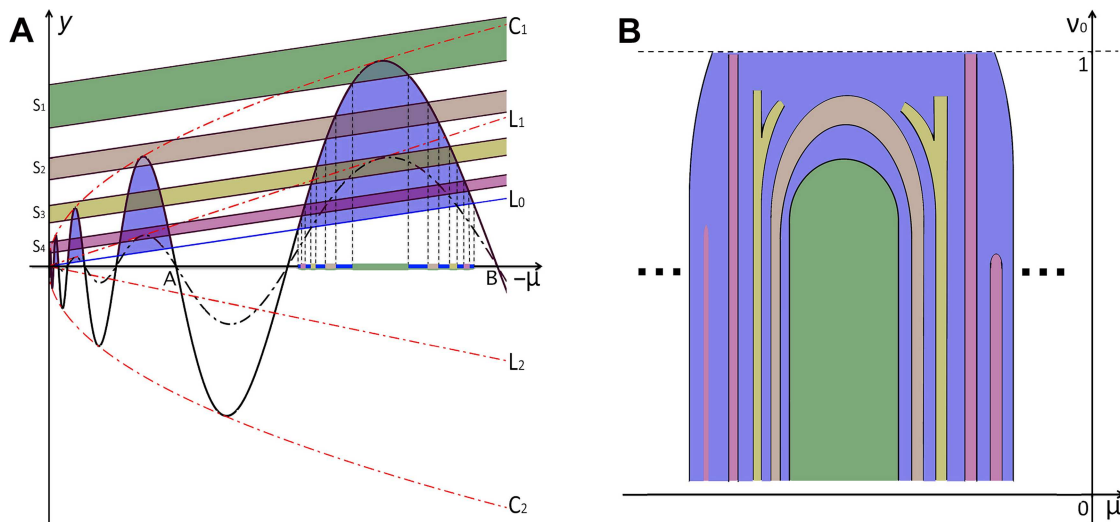
FIG. 12. $B_0 > 1$. (a) The x axis is $(-\mu)$-axis. The solid sine function is bounded by two curves $C_{1,2}$, and the dashed sine function is bounded by two lines $L_{1,2}$. The parts below the solid sine function and above the line L_0 are painted blue. Four strips S_1–S_4 line up above L_0. Their interceptions with the solid sine function are projected to the $(-\mu)$-axis. (b) Inside the blue *Pi*-bar, $(1, 0, 0)$ triple-loop pieces are drawn to match the strips in the plot (a) that they are derived from. From the middle to both the sides of the blue bar, it lists a green bar, a brown bridge, a pair of yellow "Y" pieces, a pink *Pi*-bar, and a pink ∩-bar. The width of the green bar in the middle is much larger than the rest. The width of the pieces is decreasing from the middle green bar to the side boundaries of the blue bar. The pieces on the right of the green bar are slightly wider than the pieces on the left.

onto the $(-\mu)$-axis. Four such strips S_1–S_4 are sampled in Fig. 12(a) to help us examine [100]-homoclinic bifurcations. Start with the interception of the top (green) strip S_1 and the sine-function graph: its projection is an interval on the $(-\mu)$-axis that collapses to zero as $\nu_0 \to 1$ that makes the envelope $C_{1,2}$ converge to the lines $L_{1,2}$. Its image in the (μ, ν_0)-diagram shown in Fig. 12(b) is a ∩-shaped (green) bar in the middle of the blue wide Π-bar corresponding to all homoclinic orbits starting with the [10]-code. The brown strip S_2 (located above the dashed graph of the sine function) overlaps with the blue zone (on period A–B) on two μ-intervals, which merge and then vanish when $\nu_0 \to 1$. Its image in the bifurcation diagram in Fig. 12(b) is a (brownish) bridge or arch above the green ∩-shaped bar. Let the strip S_3 cover the local maximum of the dashed sine function in Fig. 12(b). Such an intersection infers, respectively, that its corresponding images in the bifurcation diagram can be a pair of Y-shaped branches within the blue bar; see Fig. 12(b). The pink strip S_4 is placed under the local maximum of the dashed sine function. Therefore, its two overlaps cannot merge, and therefore, they correspond to a pair of narrow (pink) Π-bars or ∩-bars in Fig. 12(b). Observe that the ∩-shaped bars are located closer to the border of the enclosing blue Π-bar. As argued previously, there can be only one such green ∩-bar in the middle and a single pair of Y-shaped branches, if any, unlike the bars of other shapes for [100]-homoclinics that are not shown in Fig. 12(b) to make it visually less busy. Note that the green ∩-bar is wider than others because it is due to the overlap of the strip S_1 with the flattest part of the sine function near its local max. To conclude, let us recap that all [100]-homoclinic bifurcation objects fit inside the [10]-region. As such, one can likely notice regions associated with the green bar for [100]-homoclinics

in bi-parametric sweeps of real applications, as we will demonstrate in the second computational part of our paper. All other bars are probably too slim compared to the principle one, in the given scale, as they originate in the region where the applied sine function looks as if it is composed of nearly vertical oscillatory segments. We emphasize that the borderlines of the bars described and sketched in Fig. 12(b) correspond to the [100]-homoclinic bifurcations.

In the case $B_0 < 1$, the dashed sine-function graph resides fully outside of the blue regions. This case is somewhat similar to the case of $B_0 > 1$ except that there are no yellow $\mathbb{Y}$-shaped (due to obvious reasons by their construction) and pink Π-shaped bars in the bifurcation diagram presented in Fig. 13(b). The pink Π-like bars (not the ∩-shape) cannot exist when $B_0 < 1$ because the blue Π-shaped region morphs into the ∩-shape. One can deduct from Fig. 13(a) that all overlaps and interceptions within the blue domain first shrink and then disappear after the dashed graph is lowered further below some point.

E. One-sided [111...]-homoclinic orbits and bifurcations

A one-sided [111...]-homoclinic orbit of the saddle-focus is a longer extension of the [111]-triple homoclinic orbit as one depicted in Fig. 4(b). The corresponding 1D return maps are somewhat similar to that presented in Fig. 6(c), with the difference that it takes more forward iterates of the origin to come back to zero.

Let us consider the case where the right unstable separatrix Γ_1 of the saddle-focus of the origin orbits, say l ($l > 3$), one-sided loops before it touches the stable manifold W^s. Its symbolic representation
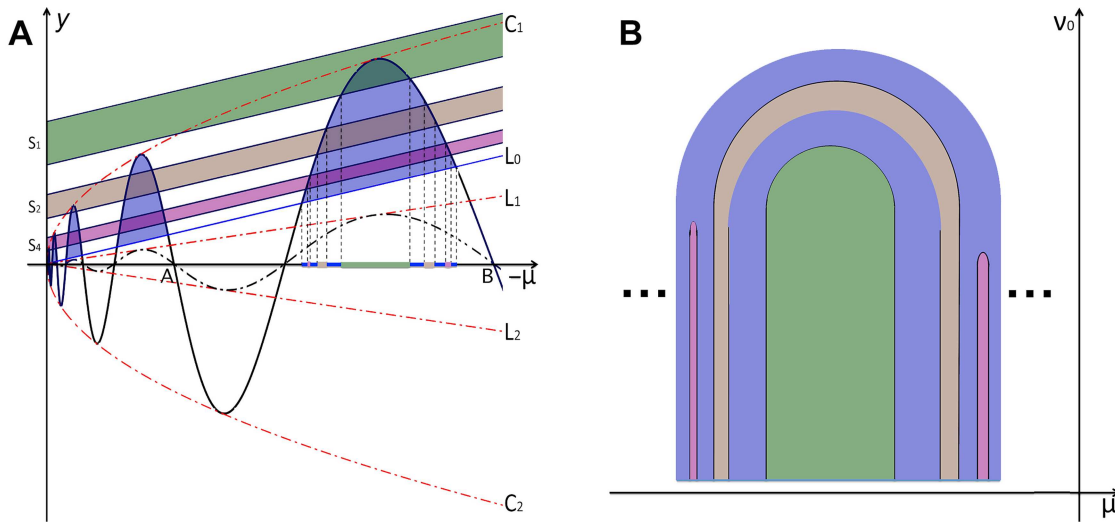
FIG. 13. $B_0 < 1$. (a) The x axis is $(-\mu)$-axis. The solid sine function is bounded by two curves $C_{1,2}$, and the dashed sine function is bounded by two lines $L_{1,2}$. The parts below the solid sine function and above the line L_0 are painted blue. Three strips S_1, S_2, and S_4 line up above L_0. Their interceptions with the solid sine function are projected to the $(-\mu)$-axis. (b) Inside the blue Π-bar, $(1, 0, 0)$ triple-loop pieces are drawn to match the strips in the plot (a) that they are derived from. From the middle to both the sides of the blue bar, it lists a green bar, a brown bridge, and a pink $\cap$-bar. The width of the green bar in the middle is much larger than the rest. The width of the pieces is decreasing from the middle green bar to the side boundaries of the blue bar. The pieces on the right of the green bar are slightly wider than the pieces on the left.

is coded as $[111\ldots 1]_l$. The system of the Poincaré map accounting for the dominant terms only (equations for φs are omitted) can be written as follows:

$$z_1 = \mu - B_0 R^{1-\nu_0}\mu^{\nu_0}\sin(\Omega_0 \ln \mu + \phi_2) + O(\mu^{2\nu_0}),$$

$$z_2 = \mu - B_0 R^{1-\nu_0}\ z_1^{\nu_0}\sin(\Omega_0 \ln z_1 + \phi_2) + O(z_1^{2\nu_0}),$$

$$\vdots \qquad\qquad\qquad\qquad\qquad\qquad (17)$$

$$z_{l-2} = \mu - B_0 R^{1-\nu_0}z_{l-3}^{\nu_0}\sin(\Omega_0 \ln z_{l-3} + \phi_2) + O(z_{l-3}^{2\nu_0}),$$

$$z_{l-1} = \mu - B_0 R^{1-\nu_0}z_{l-2}^{\nu_0}\sin(\Omega_0 \ln z_{l-2} + \phi_2) + O(z_{l-2}^{2\nu_0}).$$

Our goal here is to determine the structure of the corresponding bifurcation curves, assuming that we have already known all unfoldings for the shorter loops up to order $l - 1$. The equivalent problem is to find $R_l = \{\mu | z_{l-1} < 0\}$ given that $R_i = \{\mu | z_{i-1} < 0\}$ ($2 \le i \le l - 1$). Obviously, $z_{i-1} > 0$ ($2 \le i \le l - 1$) for $\mu \in R_l$; see Eq. (17). Therefore, R_l disjoints $\bigcup_{i=2}^{l-1} R_i$; i.e., $R_l \subset \overline{\bigcup_{i=2}^{l-1} R_i}$. This guarantees that bifurcation curves for the right l-loops fit into the gaps between all other one-sided (left/right) homoclinic orbits of lower orders.

System (17) can also be recast as

$$z_1 = \mu - B_0 R^{1-\nu_0}\mu^{\nu_0}\sin(\Omega_0 \ln \mu + \phi_2) + O(\mu^{2\nu_0}),$$

$$z_{l-1} = f_\mu(z_1),$$

where $f_\mu(\cdot)$ is a smooth function. With a constant $\nu_0 < 1$, the range of z_1, such that $z_{l-1} < 0$, can be determined through the condition $f_\mu(z_1) < 0$. It is represented by a union of countable disjoint positive ($\mu > 0$) intervals for a fixed μ value. These intervals of one-sided $[111\ldots 1]_l$ homoclinic orbits then correspond to new

colored strips such as ones shown in Fig. 10(a) for $B_0 < 1$ or Fig. 11(a) for $B_0 > 1$ that cannot overlap the strips generating similar orbits of lower orders. The shape of the corresponding bifurcation curves in the (μ, ν_0)-parameter plane is, respectively, determined by the positions of the generating strips as we discussed previously. We point out that the intervals are μ-value related, and therefore, the sides of those strips are not "perfectly" parallel in general. This observation, barely influencing the results, may nevertheless break some symmetry arrangements for long one-sided orbits. For example, in Fig. 10(b), there may be more yellow bars on the left from the purple $\cap$-shaped bar than on the right from it.

However, the intervals due to the condition $f_\mu(z_1) < 0$ may merge as $\nu_0 \to 1$ provided $l > 3$. As a result, a bridge can occur at a wrong position; for example, see the bridge associated with the yellow bar (region) in Fig. 6(b) if $l > 3$. In the case $l = 4$, this can be explained by solving system (17) for the range of μ-values for which $z_3 < 0$. We start off by solving the last equation to determine the range of z_2 such that $z_3 < 0$. This range is given by a union of the purple intervals on the z_2-axis as shown in Fig. 14(a), where the longest interval I is labeled for further explanation. The range of z_2 is then used in the second last equation $z_2 = \mu - B_0 R^{1-\nu_0}z_1^{\nu_0}\sin(\Omega_0 \ln z_1 + \phi_2) + O(z_1^{2\nu_0})$ to find recursively the range of z_1 for which $z_3 < 0$. It is represented by another union of countable intervals, among which the intervals J_1 and J_2 of z_1 are derived from the interval I of z_2 on one period of the sine function of z_1 depicted in panel (b) of Fig. 14. Finally, the range of z_1-values is then employed into the first equation $z_1 = \mu - B_0 R^{1-\nu_0}\mu^{\nu_0}\sin(\Omega_0 \ln \mu + \phi_2) + O(\mu^{2\nu_0})$ to obtain the μ-values for such $z_3 < 0$, which is a union of countable μ-intervals. Here, intervals such as k_{11} and k_{12} are derived from the interval J_1 of z_1 on one period of the sine function of μ shown in Fig. 14(c),
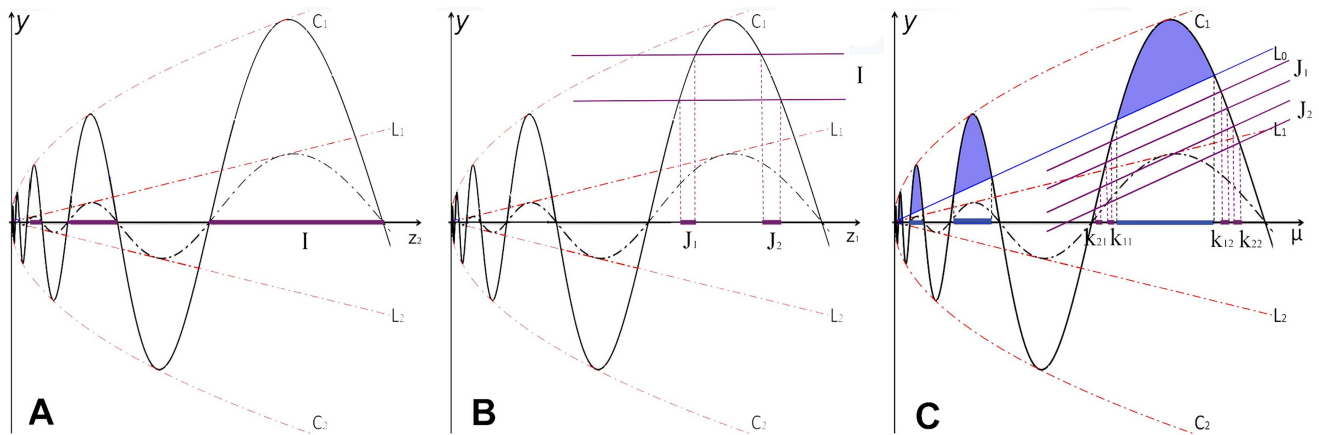
FIG. 14. (a) The positive parts of the sine function of z_2 are projected onto the z_2-axis and painted purple. One of them is notated as I. (b) A purple interval from (a), I, corresponds to a strip that intercepts the sine function of z_1. The purple intervals on the z_1-axis are the projections of the intercepts, and they are notated as J_1 and J_2. (c) The intervals from (b) correspond to two strips that intercept the sine function of μ. The purple intervals on the μ-axis are the projections of the intercepts, and they are notated as k_{11}, k_{12}, k_{21}, and k_{22}, respectively.

while intervals such as k_{21} and k_{22} are derived from the interval J_2 of z_1 on the same period. In the limit $\nu_0 \to 1$, both intervals J_1 and J_2 will merge; see Fig. 14(b). If intervals J_1 and J_2 merge before k_{11} and k_{12} do, then intervals k_{11} and k_{21} coalesce to generate a bridge section on the bifurcation curve corresponding to a [1111]-homoclinic orbit and so do k_{12} and k_{22} as well; see Fig. 14(c).

F. [100. . .]–homoclinic bifurcations

Next, consider the configuration where the 1D unstable separatrix Γ_1 first makes a single loop on one side of the stable manifold W^s and then $l - 1$ one-sided loops ($\mu < 0$) on its opposite side before it returns to the saddle-focus. Its symbolic code is hence written as $[100 \dots 0]_l$. Such an orbit may be viewed as a longer version of the inverted homoclinic connection depicted in Fig. 4(d).

The Poincaré map with only the dominant terms (equations for φs are omitted) can be written as follows:

$$z_1 = -\mu - B_0 R^{1-\nu_0}(-\mu)^{\nu_0} \sin(\Omega_0 \ln(-\mu) + \phi_2)$$
$$+ O((-\mu)^{2\nu_0}),$$
$$z_2 = -\mu + B_0 R^{1-\nu_0}(-z_1)^{\nu_0} \sin(\Omega_0 \ln(-z_1) + \phi_2)$$
$$+ O((-z_1)^{2\nu_0}),$$
$$\vdots \qquad\qquad (18)$$
$$z_{l-2} = -\mu(\pm B_0 R^{1-\nu_0})(-z_{l-3})^{\nu_0} \sin(\Omega_0 \ln(-z_{l-3}) + \phi_2)$$
$$+ O((-z_{l-3})^{2\nu_0}),$$
$$z_{l-1} = -\mu(\pm B_0 R^{1-\nu_0})(-z_{l-2})^{\nu_0} \sin(\Omega_0 \ln(-z_{l-2}) + \phi_2)$$
$$+ O((-z_{l-2})^{2\nu_0}),$$

with alternating $(+/-)$ in the equations above.

To determine the bifurcation unfolding of such homoclinic orbits, one evaluates the range, say L_l, of μ-values for which $z_{l-1} < 0$. It is evident that $L_l \subset L_{l-1}$ because $z_{l-2} < 0$ in Eq. (18). Therefore, the set $\{L_i\}_{i=2}^\infty$ decreases for any $0 < \nu_0 < 1$. System (18) can be recast as

$$z_1 = -\mu - B_0 R^{1-\nu_0}(-\mu)^{\nu_0} \sin(\Omega_0 \ln(-\mu) + \phi_2)$$
$$+ O((-\mu)^{2\nu_0}),$$
$$z_{l-1} = g_\mu(z_1),$$

where $g_\mu(\cdot)$ is a smooth function. The range of z_1-values for which $z_{l-1} < 0$ is a union of countable disjoint negative ($\mu < 0$) intervals for a fixed μ. As discussed previously, the bifurcation unfolding corresponding to $[100 \dots 0]_l$-homoclinic orbits can be illustrated using Figs. 12 and 13: the same structures re-emerge within the middle green $\cap$-shaped bar, while narrow bridges and bars re-emerge inside bridges and bars, respectively, except for the center green bar. However, starting with $l > 3$, new bridges can reside inside bars and new bars can reside within a bridge, and so forth.

G. Mixed multi-loops

Let us finally discuss mixed multi-loops—informally, those are longer homoclinic orbits that are neither solely left nor right sided at the end. Each such corresponding map will be a mix of equations from systems (17) and (18). By omitting small term μ for simplification, define these two sine functions,

$$f_0(x) = \pm B_0 R^{1-\nu_0}(-x)^{\nu_0} \sin(\Omega_0 \ln(-x) + \phi_2),$$
$$f_1(x) = -B_0 R^{1-\nu_0} x^{\nu_0} \sin(\Omega_0 \ln x + \phi_2).$$

Then, the map for a $[1\alpha_1\alpha_2 \dots \alpha_{l-1}]$-homoclinic orbit is given by

$$z_1 = f_{\alpha_1}(\mu), \quad z_2 = f_{\alpha_2}(z_1), \dots, z_{l-2} = f_{\alpha_{l-2}}(z_{l-3}),$$
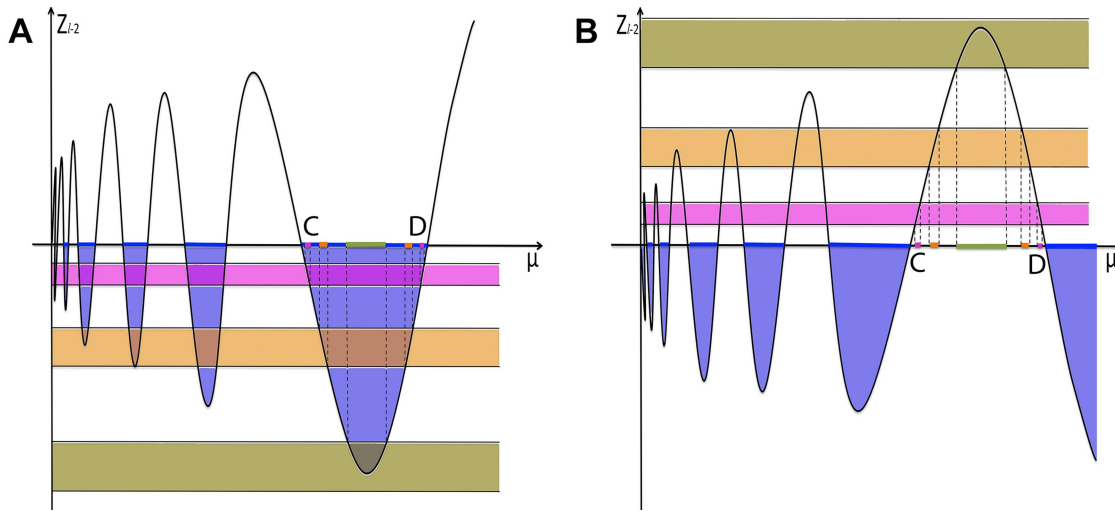$$z_{l-1} = f_{\alpha_{l-1}}(z_{l-2}), \qquad (19)$$

FIG. 15. The oscillating function is assumed to be $z_{l-2} = F(\mu)$ where $\mu > 0$. The regions of $z_{l-2} < 0$ are marked blue. Their projections on the μ-axis are marked as blue intervals. Points C and D are the end points of one of the intervals. (a) In the case of $\alpha_{l-1} = 0$, the strips of $z_{l-1} = f_{\alpha_{l-1}}(z_{l-2}) < 0$ are beneath the μ-axis. The projected intervals of the interceptions of the strips and the oscillating function are inside the blue intervals. (b) In the case of $\alpha_{l-1} = 1$, the strips of $z_{l-1} = f_{\alpha_{l-1}}(z_{l-2}) < 0$ are above the μ-axis. The projected intervals of the interceptions of the strips and the oscillating function fall in the gaps of the blue intervals.

where $\alpha_i \in \{0, 1\}$ for $1 \leq i \leq l$. Let us recast Eq. (19) as

$$z_{l-2} = F(\mu) = f_{\alpha_{l-2}} \circ f_{\alpha_{l-3}} \circ \cdots \circ f_{\alpha_1}(\mu),$$

$$z_{l-1} = f_{\alpha_{l-1}}(z_{l-2}). \tag{20}$$

We showed earlier that both $\frac{df_0}{dx}, \frac{df_1}{dx} \approx \infty$ except for within small regions near their extreme points. Therefore, $\frac{dF}{d\mu} = \frac{df_{\alpha_{l-2}}}{dz_{l-3}} \cdot \frac{df_{\alpha_{l-3}}}{dz_{l-4}} \cdots \frac{df_{\alpha_1}}{d\mu} \approx \infty$ except for small regions around critical points. Thus, the graph of $F(\mu)$ is a collection of nearly vertical line segments, which is obviously bounded. It has an abundance of extreme points because $\frac{dF}{d\mu} = 0$ where $\frac{df_{\alpha_i}}{dz_{i-1}} = 0$ ($1 \leq i \leq l-2$ and $z_0 = \mu$). Figure 15 illustrates such oscillating graphs of the function $z_{l-2} = F(\mu)$ when $\mu > 0$; it remains similar if $\mu < 0$. For the sake of structural visibility, the graph per se and monotone parts are sketched not as steep as they should be in the theory. The blue projection intervals on the horizontal axis represent all μ-values for which $z_{l-2} < 0$; i.e., they represent parameter intervals corresponding to $[1\alpha_1\alpha_2 \ldots, \alpha_{l-2}]$-mixed homoclinic loops.

If $\alpha_{l-1} = 0$, then without loss of generality, we can assume that

$$f_{\alpha_{l-1}}(z_{l-2}) = -B_0 R^{1-\nu_0}(-z_{l-2})^{\nu_0} \sin(\Omega_0 \ln(-z_{l-2}) + \phi_2).$$

The solutions satisfying the condition $z_{l-1} = f_{\alpha_{l-1}}(z_{l-2}) < 0$ are given by $z_{l-2} \in \left(-e^{-\frac{2m\pi}{\Omega_0} + \frac{\pi}{\Omega_0} - \frac{\phi_2}{\Omega_0}}, -e^{-\frac{2m\pi}{\Omega_0} - \frac{\phi_2}{\Omega_0}}\right) = I_m$, where $m \in \mathbb{Z}$ is large enough. Let the interval between I_m and I_{m+1} be notated as $J_m = \left(-e^{-\frac{2m\pi}{\Omega_0} - \frac{2\pi}{\Omega_0} - \frac{\phi_2}{\Omega_0}}, -e^{-\frac{2m\pi}{\Omega_0} + \frac{\pi}{\Omega_0} - \frac{\phi_2}{\Omega_0}}\right)$. It is easy to see that $I_{m+1}/I_m = J_{m+1}/J_m = e^{-\frac{2\pi}{\Omega_0}}$; here, $\{I_m\}$ are the colored strips accumulating to the μ-axis from below in Figure 15, where only three such strips are sampled. The projection intervals of the interception of

the colored strips with the graph $z_{l-2} = F(\mu)$ are the sought for the $[1\alpha_1\alpha_2, \ldots, \alpha_{l-1}]_l$-orbit intervals on the μ-axis; they reside inside the blue intervals corresponding to the $[1\alpha_1\alpha_2 \ldots \alpha_{l-2}]_{(l-1)}$-orbits. The $[1\alpha_1\alpha_2 \ldots \alpha_{l-2}]_{(l-1)}$-homoclinic orbits occur at the end points of the blue intervals, such as the points C and D indicated in Fig. 15. Inside the blue region $[CD]$, the green interval is much wider than the rest of the corresponding intervals because it is due to one of the extreme points of the function $z_{l-2} = F(\mu)$, whereas smaller intervals are due to nearly vertical oscillation of the given sinusoidal function.

If $\alpha_{l-1} = 1$, then the solutions satisfying the inequality $z_{l-1} = f_{\alpha_{l-1}}(z_{l-2}) < 0$ are positive ($\mu > 0$) intervals, and therefore, the intervals for $[1\alpha_1\alpha_2 \ldots \alpha_{l-1}]_l$-orbits are located within the gaps between the intervals for the shorter $[1\alpha_1\alpha_2 \ldots \alpha_{l-2}]_{(l-1)}$-orbits, as seen from Fig. 15(b). Note from this figure that the middle interval for a l-long orbit is significantly wider than the rest of such ones because it is resulted from a flatter section of the graph of the function $z_{l-2} = F(\mu)$.

It will be shown below that basic biparametric sweeps of systems with saddle-foci visibly reveal some of the largest or principle homoclinic bifurcation structures, which are likely due to such flat regions of the function $z_{l-2} = F(\mu)$, while ones due to steep oscillatory graph sections are often too narrow to be well detected and require some parameter recalling.

In a small neighborhood of an end point of each interval for $[1\alpha_1\alpha_2 \ldots \alpha_{l-2}] - (l-1)$-orbits, such as C or D in Fig. 15, the oscillating function $z_{l-2} = F(\mu)$ is nearly linear. Therefore, near the end points, the parameter intervals for the $[1\alpha_1\alpha_2 \ldots \alpha_{l-1}]_l$-homoclinic orbits hold a scalability ratio $e^{-\frac{2\pi}{\Omega_0}}$ for both width and distance, following from the relationship: $I_{m+1}/I_m = J_{m+1}/J_m = e^{-\frac{2\pi}{\Omega_0}}$.

The following theorem concludes our arguments and reckoning above:
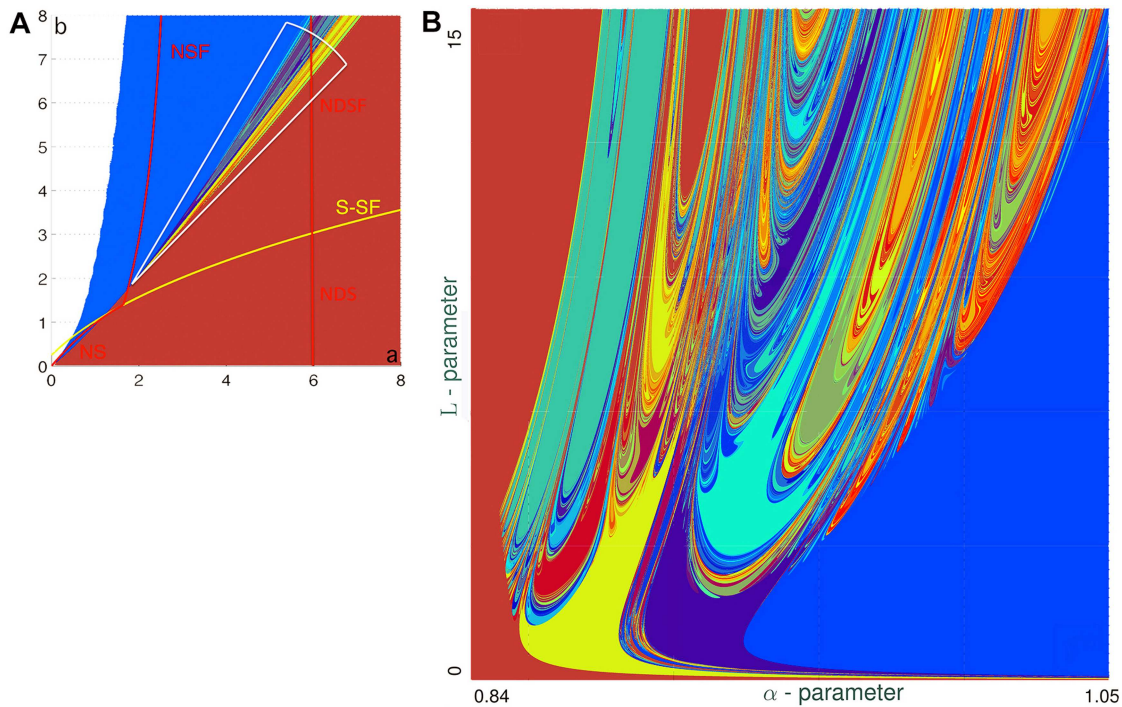
FIG. 16. (a) Short bi-parameter sweep of the cubic Chua model using the original parameters. The curves NSF and NS correspond to zero saddle value $\sigma_1 = 0$ or $\nu = 1$ ($\nu > / < 1$ on the left/right of these curves); NDSF and NDS correspond to zero divergence $\sigma_2 = 0$ or the saddle index $\nu = 1/2$ at the saddle-focus. The yellow S–SF curve marks the transition of the origin between a saddle and a saddle-focus. All three curves cross near the point (1.6458, 1.3934). The solid color regions correspond to trivial dynamics with constant kneadings. The narrow colorful wedge is the region of double-scroll chaotic dynamics due to homoclinic bifurcations. The sector bounded by the white curves with the tip point near (1.8623, 1.8743) is unfold in panel (b). (b) Short bi-parameter sweep of the model with new (α, L)-parameters revealing the stunning complexity and universality of homoclinic bifurcations of the Shilnikov saddle-focus at the origin of the Chua model; here, [2-12] and [6-15]-long binary sequences are used for A and B, respectively.

Theorem 2. *Under the conditions of Theorem 1, in the (μ, ν_0)-parameter space, all bifurcation curves corresponding to $[\alpha_1\alpha_2\ldots\alpha_l]_l$- homoclinic orbits, where $\alpha_i \in \{0, 1\}$, $1 \le i \le l$, (i) are embedded between the bifurcation curves corresponding to $[\alpha_1\alpha_2\ldots\alpha_{(l-1)}]_{(l-1)}$-homoclinic orbits provided that $\alpha_l = 0$ or (ii) they reside within the gaps between the bifurcation curves corresponding to $[\alpha_1\alpha_2\ldots\alpha_{(l-1)}]_{(l-1)}$-homoclinic orbits if $\alpha_l = 1$. The scalability ratio for both the widths and the distances of the curves is given by $e^{-\frac{2\pi}{\Omega_0}}$, near the bifurcations of $[\alpha_1\alpha_2\ldots\alpha_{(l-1)}]_{(l-1)}$-orbits.*

III. HOMOCLINIC BIFURCATIONS IN THE SMOOTH CHUA CIRCUIT

Let us get back to the smooth Chua model (1) and discuss the bifurcations of its equilibria. The summary can be found in the (a, b)-bifurcation diagram shown in Fig. 3. Recall that the system (1) has three equilibrium states located at $O(0, 0, 0)$, $O_1(-1, 0, 1)$ and $O_2(1, 0, -1)$. The curve labeled by NSF, standing for "neutral" saddle, with the saddle index $\nu = 1$ or zero saddle value $\sigma_1 = 0$, at the origin is given by $b = \frac{(a^2 - 33a + 36)(a-6)}{36(3-a)}$. The NDSF curve of O is given by $a = 6$; this abbreviation stands for the saddle-focus at 0 with zero divergency $\sigma_2 = 0$ or $\nu = 1/2$ for saddle-foci; the sum of

all three characteristic exponents is negative below this level where the system remains dissipative, whereas it becomes positive above it, making the space volume expand near the origin. While there is no curve corresponding to $\nu = 0$ at the origin O, however, the curve for $\nu = \xi$ at O is given by $b = \left(\frac{7a(a-6)}{12} - \frac{\xi(a-6)^3}{36(1-2\xi)^2}\right)/(a\xi - 3)$ for $\xi \ne 1/2$ and $0 < \xi < 1$. It has an asymptote $a = 3/\xi$, and therefore, we can approximate the curve $\nu = \xi$ using $a = 3/\xi$. The curve $\mu = 0$ defined for modeling the 1D map (9) must be associated with the $H8$-curve in Fig. 3 that corresponds to the primary homoclinic bifurcation in the system (1), as illustrated in Fig. 5. It is easy to see the correspondence between the (μ, ν_0)-parameter plane and the (a, b)-parameter plane; therefore, the system (1) is an ideal example to showcase the theory built in Sec. II.

A. Symbolic computational method

Bi-parametric sweepings of the system (1) are done by using the computational methods originally introduced in our earlier papers[7,9] with a few changes; see also the following papers.[8,10,16-19]

We follow the trajectory that initiates from the right unstable separatrix Γ_1 of the origin and record "1" when it loops around the right equilibrium $O_2(1, 0, -1)$ and "0" when it loops around the
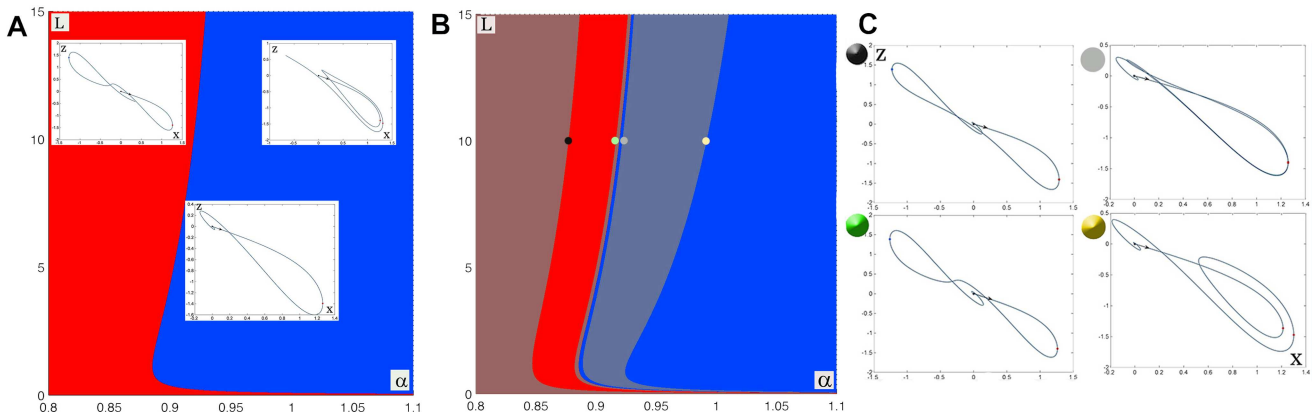
FIG. 17. (a) (α, L)-biparametric sweep using [1-2]-long binary sequences reveals the primary homoclinic bifurcation curve [1], separating the red and blue regions (see a homoclinic trajectory in the bottom inset). The trajectories in the red region have symbolic encoding of the form $\{1, 0, \ldots\}$ (see trajectory in the top left inset) and those in the blue region have $\{1, 1, \ldots\}$ (top right inset). (b) [1-3]-long binary sequence reveals two further homoclinic bifurcation curves, [10] (with the black and green points) and [11] (with the gray and yellow points). The positions of the black, green, gray, and yellow points in the $\alpha - l$ plane are given by (0.876898493756, 9.995), (0.91631772114, 9.995), (0.921727874, 9.995), and (0.991649733, 9.995), respectively, and the corresponding homoclinic orbits are shown in (c).

left equilibrium $O_1(-1, 0, 1)$; see Fig. 2(a). Alternatively, we can use x-traces to convert into binary sequences so that "1" stands for a positive maximum greater than 1 and record "0" when x reaches a negative minimum smaller than -1; see Fig. 2(b). We can skip the very first symbol as it is always "1" by construction. Such a binary sequence, also known as a kneading sequence, is recorded for a pair of a- and b-parameter values to create a bi-parametric sweep. Next, the binary sequence is converted to a decimal number by using this following rule:

$$K(a, b) = \sum_{n=i}^{j} \kappa_n \, q^{(j-n+1)},$$

where $\{\kappa_n\}_{n=i}^{j}$ is the corresponding binary sequence with $\kappa_n = \{0, 1\}$ and i, j are positive integers with $i \leq j$ (the first $i - 1$ binary symbols are skipped). $0 < q < 1$ is chosen for such a formal power series to converge. In this study, we set $q = 0.5$ and keep $K(a, b)$ in the range $[0, 1]$. This decimal number is known as the kneading invariant. By construction, the K-values range between 0 and 1. The boundary values are set by the periodic sequences $\{\overline{0}\}$ and $\{\overline{1}\}$, respectively, for infinitely long sequences.

Numerical integration is performed using a 4th-order Runge–Kutta method with a fixed step-size. The computation of trajectories across different parameter values is parallelized using graphic processing units (GPUs). Data visualization is done in Python. A colormap takes K-values into 2^8 discrete bins of RGB-color values, assigned from 0 through 1 for each channel of red, green, and blue colors in decreasing, random, and increasing order, respectively. With such a colormap, we can assign a unique color to a single kneading invariant to produce a *colorful* sweep with 1000×1000 points in the biparametric plane, as shown in Figs. 16–26. Parameter values that produce topologically similar trajectories result in identical sequences $\{\kappa_n\}$ and, therefore, have the same K-values and colors in a biparametric sweep. We employ two symbolic approaches using (i) short, $1 \leq i \leq j \leq 10$, binary sequences to detect a plethora

of homoclinic bifurcations (see Figs. 16–24) and (ii) long, typically $600 \leq n \leq 1000$, ones to detect stability windows within chaos-land in the parameter sweeps (see Fig. 26). The computation of these trajectories is massively parallelized by running on separate GPU threads using CUDA. On a Tesla K40 GPU-powered workstation, a 4000×4000 resolution sweep takes from merely a few seconds to several minutes depending on the sequence length and the sweep resolution.

Let us first discuss the first approach. By construction, a borderline between distinct colored regions in sweeps employing short sequences is a homoclinic bifurcation curve in the parameter space. In theory, one can detect up to 2^{10} homoclinic bifurcations in such sweeps with 10 binary symbols.

Figure 16(a) represents a short (a, b)-parameter sweep of the cubic Chua model (1). It is overlaid with the neutral saddle-focus bifurcation NSF-curve, the saddle-to-saddle-focus transition (S–SF)-curve, and the zero divergence NDS/NDSF curve ($\nu = 1/2$). Of our interest is the narrow wedge in the diagram that embraces many homoclinic bifurcation curves (of various colors), thus suggesting the onset of chaotic dynamics as it is located between the NSF and the S–SF curves, where the origin is the Shilnikov saddle-focus with $\nu < 1$. The solid colors, blue and brown, indicate the regions of simple, Morse–Smale dynamics with stable equilibria and/or periodic orbits; see trajectory snapshots on the pathway $b = 6$ in Fig. 3.

For a better look inside the wedge, we will apply a parameter transformation to widen this region. First, let us identify a sector in Fig. 16(a), which is bounded by white curves, with its tip located at $(1.8623, 1.8743)$. Let us introduce two new polar-coordinates/parameters: α and L; here, α is an angular variable inside the sector and the positive axis and L is the length of the sector, i.e., the radial variable. The transformation is then given by

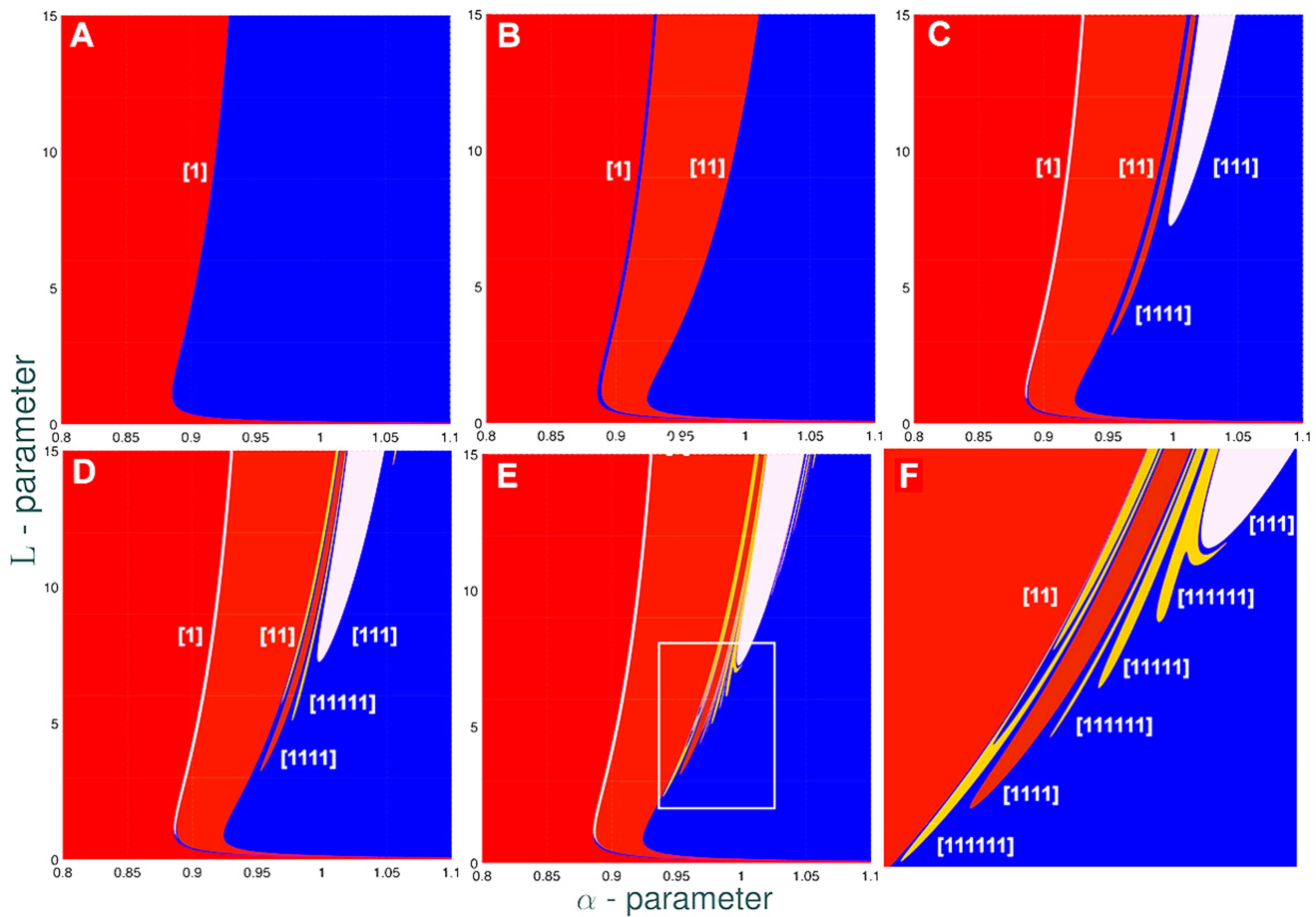$$a = 1.8623 + L\cos(\alpha), \quad b = 1.8743 + L\sin(\alpha), \quad (21)$$

FIG. 18. A series of biparametric sweeps with longer binary sequences reveal an increasing hierarchy of bifurcation curves of one-sided homoclinic orbits beginning with (a) the primary one; (b) two identified curves for double [11]/[00]-loops; (c) bifurcation curves for triple [111]/[000] (wide white), and [1111]/[0000]-orbits (narrow dark red) and longer one-sided orbits in (d) and (e). (f) Magnified inset from (e) revealing various ∩-shaped and "Y"-shaped secondary bifurcation curves (here, corresponding to [111111]-homoclinic orbits) as predicted by the theory.

where $\alpha \in [0.8, 1.05]$ and $L \in [0, 15]$. The sweep using new (α, L)-parameters is shown in Fig. 16(b). It shows a plethora of bifurcation curves representing various one-sided and mixed homoclinic orbits. In what follows, we will attempt to figure out the ordered intricacy and universality of the organization of such bifurcation curves in the Chua model and other such $\mathbb{Z}_2$-symmetric systems.

Figure 17(a) represents the shortest sweep of length 2 to reveal the primary homoclinic bifurcation H_1 [1] of the saddle-focus at the origin. It occurs on the borderline of two regions: red and blue where the binary sequences start with [10...] and [11...], respectively. Increasing the length lets us disclose at least two pairs of bifurcation curves in the parameter diagram [Fig. 17(b)], corresponding to the double homoclinic loops [10] and [11] [see Fig. 17(c) for phase trajectories]. Arguably, they all have a U-shape, stretched horizontally. These bifurcation curves for double loops lie on both sides of the primary one H_1 ($\mu = 0$), as the sweep discloses. Here, the left-side of H_1

corresponds to $\mu < 0$ and the right side corresponds to $\mu > 0$ if we refer to the modeling 1D maps studied above. Figure 17(b) detects well two principal bifurcation curves (labeled with black and yellow dots) away from H_1 on either sides (two other curves labeled with green and gray dots are immediately next to H_1 and are not seen clearly). They correspond to the largest blue ∪-shaped bars in Figs. 7(b) or 10(b). The rest of the countably many curves are too close to H_1 to be identified in the sweep of the current scale; we discussed the reasons in Sec. II above.

The sweep utilizing progressively longer, [2–4], binary sequences exposes bifurcation curves corresponding to various triple loops and so on. The longer the kneading sequence used, the higher the order of homoclinic orbits and bifurcation curves that can be revealed. For example, the sweep shown in Fig. 16(b) utilizes symbolic subsequences of the [6–15]-range, revealing several thousands of bifurcation curves, limited due to scaling factors.
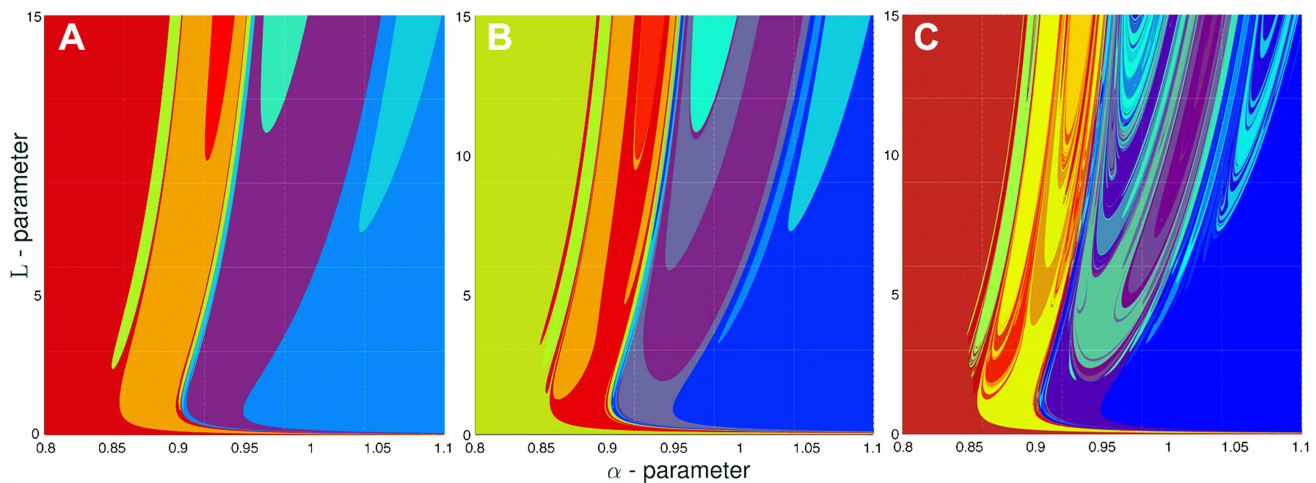
FIG. 19. Three snapshots of the (α, L)-biparametric sweeps of the Chua system with increasing length of symbolic sequences from [2,4] in (a) to [2,5] and [2,9] in (b) and (c), respectively, reveal the complexity and organization of mixed multi-loop homoclinic bifurcation curves of the system.

B. [111...] or one-sided homoclinic orbits and bifurcation curves

The detailed sweep in Fig. 16(b) discloses bifurcation curves corresponding to all homoclinic orbits of the saddle-focus, using [6–15]-long binary sequences. Next, we would like to see what the typical bifurcation unfolding of the generic Shilnikov saddle-focus may look like. To do so, we modify the approach to focus only on one-sided homoclinic orbits and the corresponding bifurcation curves. This is accomplished by obtaining for each (α, L)-parameter pair, symbolic sequences containing the same symbol (say, [111 ...]) until the very first occurrence of the other symbol ("0"). If the number of "1"s in a symbolic sequence for some one-sided orbit is n, then the corresponding kneading invariant is defined as $K(\alpha, L) = n/r$, provided r is the total length of such sequence.

The results of such one-sided symbolic approach are summarized in Fig. 18. Using sequences up to two symbols long, we identify the primary homoclinic bifurcation shown in Fig. 18(a). With an additional symbol, the well-visible [11]-bifurcation curve in Fig. 18(b) is revealed. This curve corresponds to the largest and furthest blue ∩-shaped bar on the right in Fig. 7(b) or 10(b). The two white U- or ∩-shaped regions seen in Fig. 18(c) are due to the right triple [111]-orbits that correspond to the large purple ∩-bar in the center of Figs. 9(b) and 10(b), which are due to the intersections of the sine function with the strip S_1 in Figs. 9(b) and 10(a). All other such triple orbits occur near the primary one, and their bifurcation curves are hardly detected in such sweeps at the given scale, as discussed in Sec. II C. The bifurcation curves corresponding to [1111]-homoclinic orbits fill in the gaps between those for triple orbits; see Fig. 18(c). This is also the case with the narrow bifurcation curves for longer orbits, see Figs. 18(d) and 18(e), which are harder to observe in sweeps at the given scale. To remedy this, we magnified a small region [the white inset in Fig. 18(e)] of interest near the curve terminals in Fig. 18(f). According to its relative position, it must be derived from the strip S_3 in Fig. 10(a).

This magnified sweep can well depict a pair of visible yellow regions whose boundaries correspond to [111111]-homoclinic orbits. There is a single (yellow) "Y"-shaped region for the same [111111]-orbits near the [111] U-shaped zone, similar to ones due to the strip S_1, which are shown in Figs. 10 and 11. One can also see a bridge on the top of a yellow piece that was determined earlier to be derived from the strip S_4 in Fig. 10, as was discussed in Sec. II.

C. Mixed multi-loop homoclinic bifurcation curves

Figure 19 demonstrates four progressive (α, L)-parameter sweeps of the Chua model with an increasing length of symbolic sequences: from [1,4] to [1,7]. Shorter sweeps are depicted in Figs. 17(a) and 17(b) revealing the primary and double homoclinic bifurcations of the central saddle-focus in the system. One can see that the double bifurcation curves reside on either side of the primary one. In these parametric sweeps, the bifurcation curves for longer orbits squeeze into the gaps between or fall inside the lower order bifurcation regions. It seems likely that the most principle bifurcation structures and boundaries, which are visible in all the sweeps, are derived from the strips that intercept the flat extreme point regions, such as the green strip in Fig. 10. All other countably many curves according to the analysis done in Sec. II are too slim to be identified. Nevertheless, some interesting details can yet be pointed out. For example, the progression from panel (a) to panel (b) of Fig. 19 reveals two visible bridges near the bifurcation curve for double one-sided orbits, which would have to be derived from the strip S_2 in Figs. 10 and 11. There are also two symmetric ∩-shaped bars added to the picture in the left double-loop HB piece, and they must be derived from the strip S_4 from the same theoretical constructions. One can see many such similarities between the theoretical and computational bifurcation diagrams.

We may assume that further detailed discussion of the bifurcation unfolding, with the quickly growing complexity presented in Figs. 16(b) and 19, is unnecessary or even unrealistically
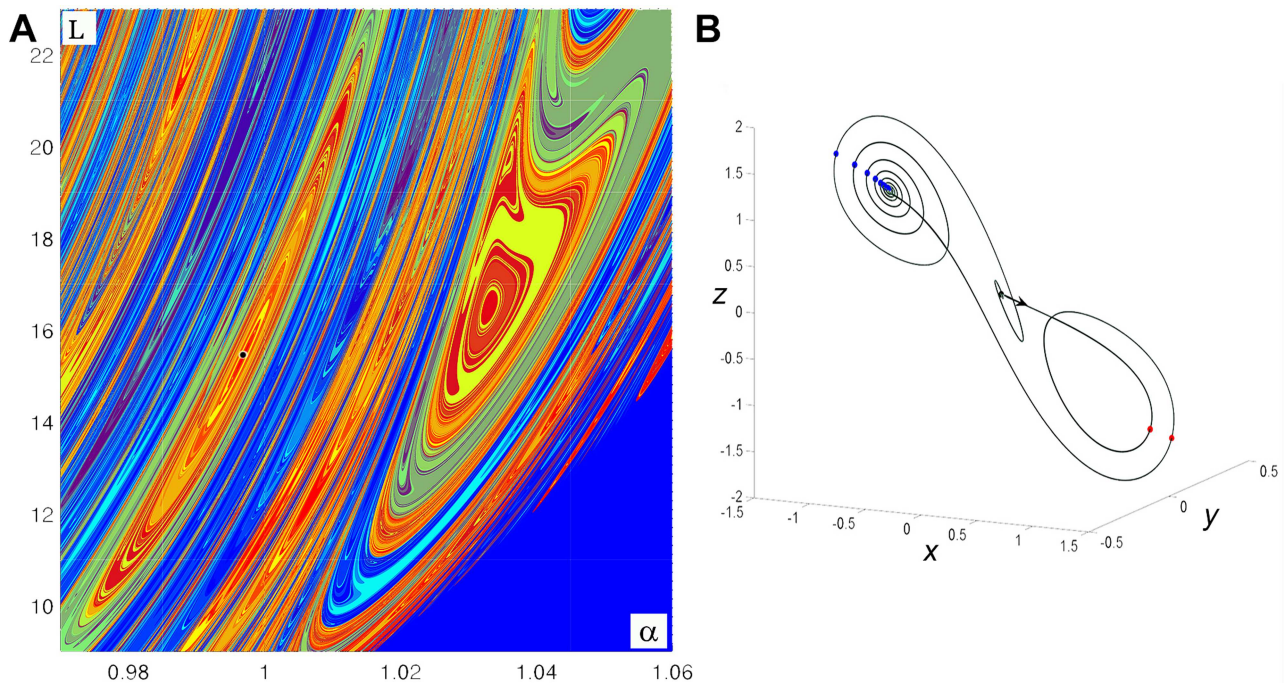
FIG. 20. (a) A biparametric [7-17]-long sweep made of 42 sub-panels, each with 1000 × 1000 points, showing a T-point—the black dot (0.9971, 15.2888)—at the center of the characteristic spiral. (b) A two-way heteroclinic connection at the T-point (black dot in panel A): the separatrix Γ_1 of the saddle-focus at the origin O terminates at the left saddle-focus O_2, whereas an outgoing trajectory spiraling away from O_2 converges to O.

comprehended, as Ovsyannikov, Shilnikov's student and co-author,[30,31] joked more than three decades ago: "the saddle-focus is as inexhaustible (infinite) as the electron."

IV. BYKOV T-POINTS

Figure 20(a) presents another bi-parameter sweep of the Chua model. There are two new patterns in it that have not been well recognized in the other sweeps. The first pattern is a family of (yellow-red) nested closed circles, while the second pattern is due to several characteristic spirals stretched nearly vertically in the sweep. Such a spiral is the distinguished feature converging to the so-called T-point of codimension-two, corresponding to a two-way heteroclinic connection between a saddle and/or saddle-foci of different topological types. Such a heteroclinic connection between the central saddle-focus O of (2,1)-type at the origin and the left saddle-focus O_2 of (1,2)-type is shown in Fig. 20(b). Due to the symmetry, there are always two such connections. In this phase space projection, the 1D unstable separatrix Γ_1 of O and one of two 1D stable separatrices of O_2 coincided in the 3D phase space of the Chua model. This constitutes a one-way heteroclinic connection. Meanwhile, the 2D unstable manifold of O_2 and the 2D stable manifold of the origin cross along a trajectory connecting both the saddle-foci; see Fig. 20. This makes this heteroclinic connection a two-way one. According to the original research by Bykov,[38,62] the occurrence of a single primary T-point implies that there are

infinitely many T-points nearby. A few other T-points with characteristic spirals can also be recognized in the sweep in Fig. 20(a). Moreover, by virtue of the theory, unlike the case of the T-point of the saddle—saddle-focus connection with a single principal spiral terminating in it, the unfolding of the T-point of two saddle-foci includes two "transverse" spirals in the parameter plane, each representing the bifurcation curve of either Shilnikov saddle-focus with a homoclinic orbit with incrementally increasing the number of turns around the other saddle-focus as the center of the spiral is approached with each revolution. As the Chua model is a dissipative system, we cannot employ our method to detect such bifurcation curves related to the saddle-foci $0_{1,2}$ to integrate solutions backward in time. Alternatively, one should use parameter continuation software, such as MatCont, that is designed to solve both initial- and boundary-value problems to continue unstable solutions. We reemphasize that according to Bykov,[63] there are infinitely many T-points in a symmetric saddle-focus system such as the Chua model and various Lorenz-like systems; see Refs. 7–10 and 16 including 3D parameter space reconstructions near T-points examined in Ref. 19.

Concerning the nested circle pattern in Fig. 20(b), this happens when the bi-parameter sweep cuts a higher, say, three-dimensional parameter space not throughout a T-point (it becomes a space line in 3D) but only slices 2D spiraling surfaces wrapping around it at a different angle; see more in Ref. 19. This is also called a "non-transverse" T-point in Ref. 64.
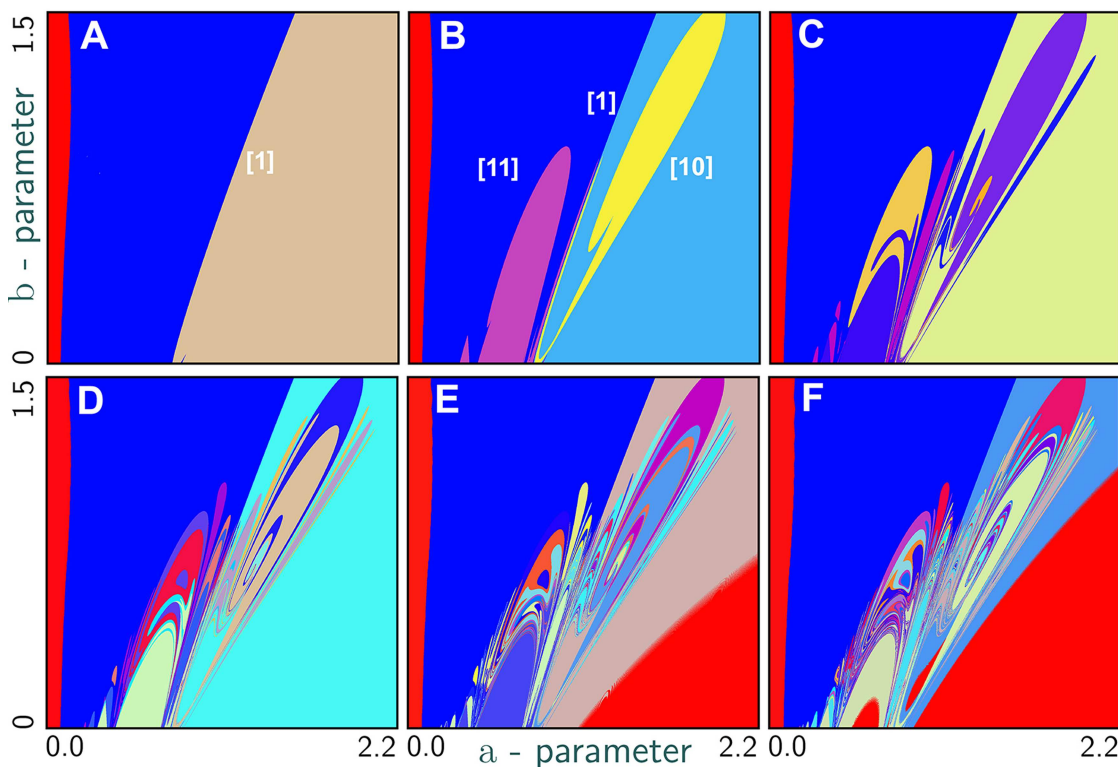
FIG. 21. Bi-parametric sweeps with the increasing length of symbolic encoding, from 2 to 9 in panels (a)–(f), respectively, of the separatrix Γ_1 of the saddle-focus at the origin in the ACST-model using the original (a, b)-parameters. In the red regions, the 1D unstable separatrix Γ_1 of the origin escapes to infinity after a few or multiple turns around the saddle-foci $O_{1,2}$. One can observe several formed and forming T-points with characteristic spirals and nested circles around. A vicinity of the T-point is magnified in Fig. 25(a).

V. SYMMETRIC ACST-MODE WITH CUBIC NONLINEARITY

Let us finally consider a second example to showcase the symbolic approach and to disclose the universality of homoclinic and heteroclinic patterns due to Shilnikov saddle-foci. The model (2) is the $\mathbb{Z}_2$-symmetric extension of the generic asymptotic normal form, called the quadratic ACST-model,

$$\dot{x} = y, \quad \dot{y} = z, \quad \dot{z} = -y - bz + ax(1-x), \tag{22}$$

with $(a\,b) > 0$ being bifurcation parameters, describing locally occurring bifurcation in systems, near an equilibrium state with three zero characteristic exponents. Using the cubic term x^3 instead of x^2 in system (22), let us worry less, computationally, about homoclinic orbits running away from the Shilnikov saddle-focus at the origin. Still, we can examine the basic homoclinic bifurcations in full generality if we focus on one-sided orbits only in Eq. (2). This model also has three equilibria: the origin O can be saddle-focus of the topological (2,1)-type, while $O_{1,2}(0, 0, \pm 1)$ becomes saddle-foci of the (1,2)-type after a supercritical Andronov–Hopf bifurcation following the period-doubling cascade initiating the onset of chaos in it; see Fig. 3.

Several snapshots of bi-parametric sweeps with an increasing, from 2 to 8, length of symbolic encoding of the ACST-model with the original (a, b)-parameters are shown in Fig. 21. The area painted in red color in panel (e) is where the solutions of the model escape to infinity. One can observe from this figure that the $\cap$-shaped bifurcation curves of longer homoclinic orbits are revealed in matching pairs in a similar fashion as the smooth Chua model. The sweeps in Figs. 21(d) and 21(e) also disclose the location of several formed and forming T-points with their characteristic spirals and nested circles corresponding to heteroclinic connections between the saddle-foci.

Following the same approach as before, by introducing two new parameters, c and d with the aid of this transformation,

$$a = 0.24 + 1.76c + 0.55d, \quad b = 1.24c + 0.81d, \tag{23}$$

we can widen up the parameter sector to provide better insights into the homoclinic unfoldings due to asymmetric one-sided or generic orbits and those due to the symmetry of the model.

With the new parameters, the sweeps better illustrate the intrinsic organization of the Shilnikov homoclinic bifurcations in the cubic ACST-model. Let us first consider the series of sweeps shown in Fig. 22 representing the building hierarchy of the bifurcation unfolding representing one-sided [11 . . .] homoclinic orbits in the
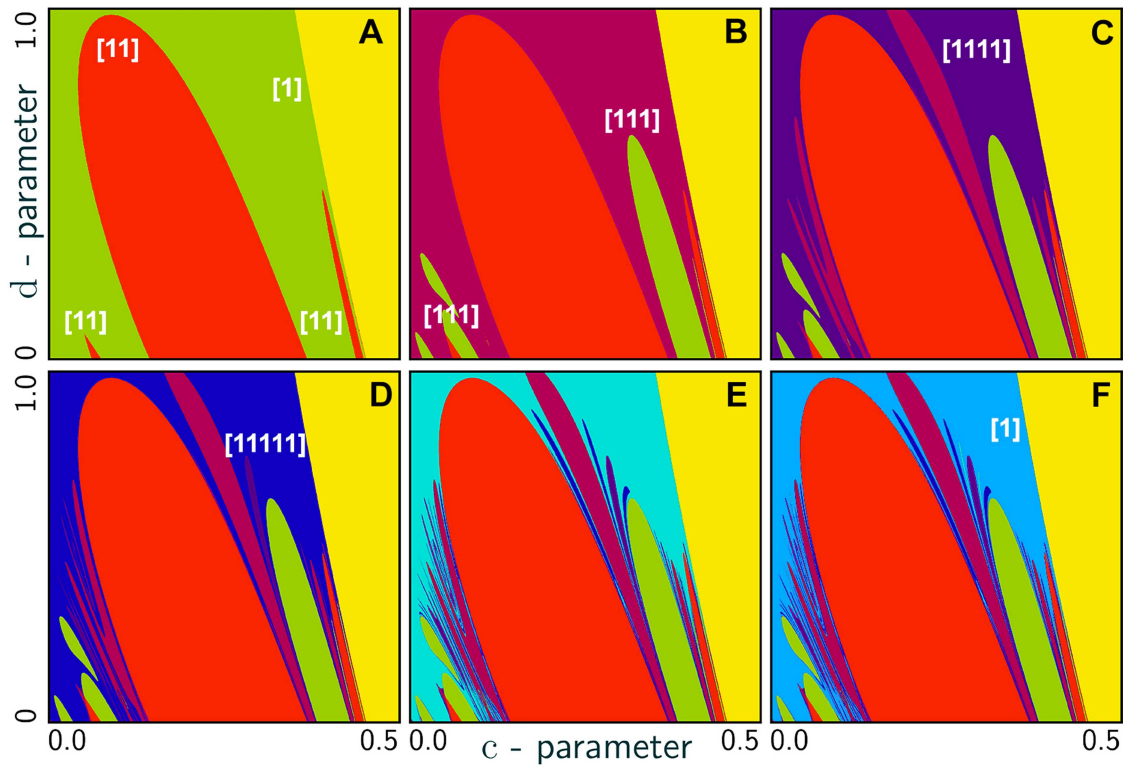
FIG. 22. The biparametric sweeps of the cubic ACST-model with the new (c, d)—parameters revealing the ordered intricacy of homoclinic bifurcations of one-sided homoclinic orbits encoded with [111 . . .], using [3,3]- through [3,8]-long symbols from (a) to (f). Panels (b)–(f) depict how new bifurcation curves corresponding to longer homoclinic orbits progressively fill in the gaps between ones corresponding to the shorter one-sided homoclinic orbits, to the left of the primary [1]-curve, as follows from the theory; compare with Figs. 10(b) and 11(b) and the sweep for the Chua circuit in Fig. 18.

$\mathbb{Z}_2$-symmetric model (2), which would be equivalent to the generic ones occurring in system (22) with x^2-term. Figure 22(a) depicts the primary [1]-homoclinic bifurcation curve and three ∩-shaped ones (red boundaries) corresponding to the double [11]-orbits, while Fig. 22(b) adds up several (green) curves corresponding to the triple [111]-homoclinic orbits. One can observe from the next panels in Fig. 22 that the new ∩-shaped curves for longer one-sided orbits such as [1111] and so on fit in between the preceding ones corresponding to shorter orbits, as predicted by the theory; see Figs. 7(b) and 11(b) above and a similar sweep in Fig. 18 for the Chua circuit.

Next, let us discuss how the ∩-shaped [11]-regions in Fig. 22(a) are populated by bifurcation curves corresponding to left-sided homoclinic orbits encoded as [1100 . . .]. This is illustrated by a series of such sweeps in Fig. 23 of an increasing length to reveal up to six [0]s following the initial block [11]. The corresponding symbolic ranges are given by [3,4]- through [3,9]. One can see from the initial sweep in Fig. 23(a) that the largest [11]-region now includes two (yellow) islands whose boundaries correspond to the [110]-homoclinic orbits. The lower one is of the ∩-shape, while the one above is of the Y-shape, just like in the bifurcation sketch in Fig. 12(b). As the sweeping length is increased, more complex bifurcation structures for orbits such as [1100] and so on start filling in

the spaces between the matching borders for shorter orbits. We let the reader to figure out a self-similar order, if any, of this puzzle.

Finally, the sweeps in Fig. 24 amalgamate step-by-step all identified bifurcation structures corresponding to one-sided and mixed homoclinic orbits in the cubic ACST-model. While one can easily follow the first building steps in panels 24(a)–24(d) incorporating large structures discussed above, the last two panels [24(e) and 24(f)] can only be inspected visually by merely stating that they incorporate smaller self-similar ones corresponding to more complex orbits. In addition, one can also spot several families of nested circles due to non-transverse T-points for heteroclinic connections that interfere with our primary targets—homoclinic bifurcations—to further recursively complicate this overall global bifurcation unfolding, beyond feasible limits.

Figure 25(a), concluding this section, magnifies the vicinity of the primary Bykov T-point shown in Figs. 21(d)–21(f) near $(0.642, -0.15)$ in these new (c, d)-parameters introduced in Eq. (23). This figure also reveals multiplicity of secondary T-points squeezed between the spirals corresponding to homoclinic orbits with shorter encodings [1000 . . .] of the origin. The demarcation curve ending at the T-point is an artifact due to the coding and color-map algorithms: with each revolution, the number of zeros in the binary
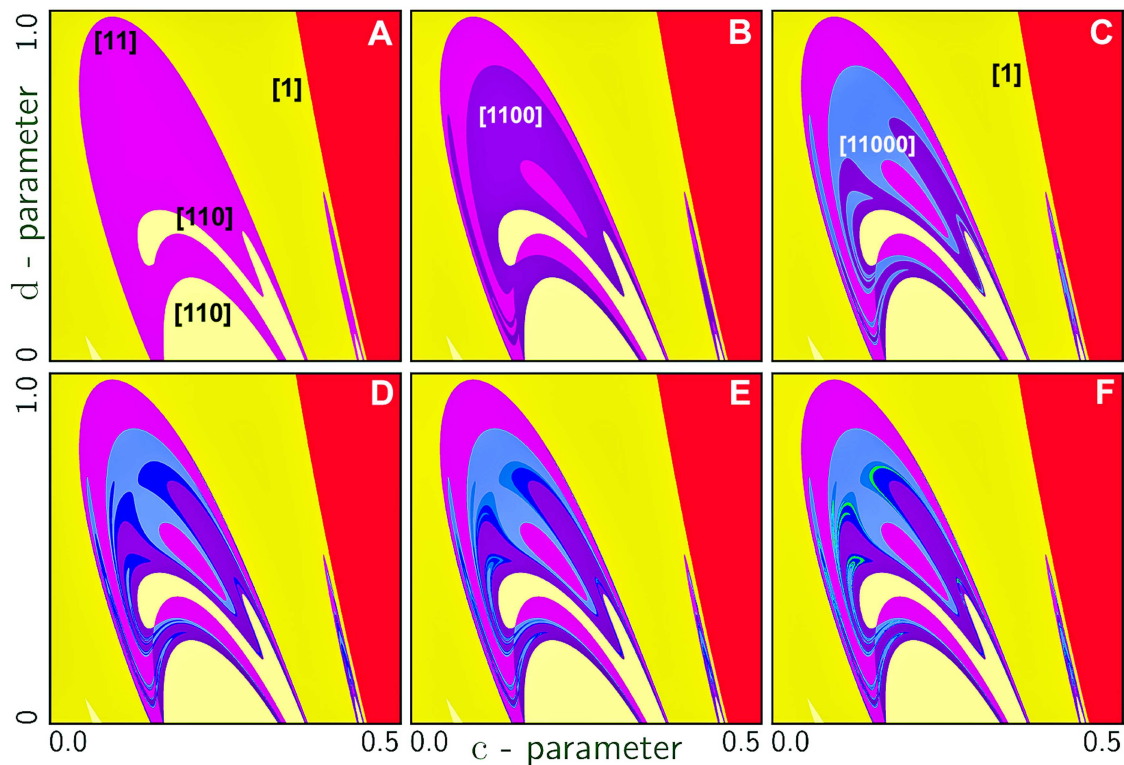
FIG. 23. The biparametric sweeps of the cubic ACST-model with the new (*c*, *d*)-parameters revealing how the bifurcation curves of longer "left"-sided [110 . . .] homoclinic orbits are nested within the larger structures corresponding to double [11]-orbits, beginning with [110], [1100], and [11000] in (a)–(c). Panels (b)–(f) depicting how new left-sided bifurcation curves corresponding to longer homoclinic orbits progressively fill in the gaps between ones corresponding to the shorter one-sided homoclinic orbits below the [11]-curve, as follows from the theory; compare with the theoretical diagrams in Figs. 10(b) and 11(b) and the bi-parametric sweep of the Chua circuit in Fig. 18. Here, panels (a)–(f) are obtained using symbolic sequences [3,4]- through [3,9].

sequence increases incrementally by one, which makes the color change.

VI. LONG-TERM SYMBOLIC APPROACH TO DETECT STABILITY WINDOWS WITHIN CHAOS-LAND

We have recently developed an approach called the "Deterministic Chaos Prospector" (DCP) (available as an open source toolkit at https://bitbucket.org/pusuluri_krishna/deterministicchaosprospector/) whose significance for the study of homoclinic bifurcations is that not only it can reveal the short term transient dynamics and the underlying homoclinic, heteroclinic, saddle, and T-point spiral structures, but it can also be employed to examine the long-term behavior and to detect the regions of simple dynamics due to stable equilibria and periodic orbits and ones corresponding to chaos in the Chua, ACST, and other systems such as the various Lorenz-like and Rössler models.[16–19,46] The underlying idea is that a trajectory integrated long enough for some parameter values may eventually converge to an exponentially stable attractor with a non-changing symbolic encoding that occupies some existence region filled out with a solid color in the parameter sweep (see Fig. 26). On the contrary, by virtue of structural instability, this is not the case for the

(grayish) regions of deterministic chaotic dynamics. Such sweeps are obtained by computing trajectories from the same or different initial conditions long enough so that after skipping some initial transients, we can still generate sufficiently long binary sequences, say, of [600–1000]-length.

The sweeps are constructed by first analyzing each long binary sequence (after omitting a transient) to detect periodicity. Periodic sequences (corresponding to simple, i.e., stable dynamics and structurally stable) of different periods are marked with different solid colors in the sweep. Aperiodic sequences (complex, structurally unstable dynamics) representing chaotic trajectories are processed using the Lempel–Ziv (LZ) compression algorithm to measure their complexity.[65] Greater LZ-complexity indicates greater instability and is shown in darker gray. Further details of DCP can be found in Refs. 16, 19, and 46.

The long-term sweeps of the Chua circuit and the ACST-model are demonstrated in Figs. 26(a) and 26(b), respectively. Both reveal exceptionally well a plethora of stability windows (solid color) with distinct periodic orbits and regions of chaos shown in gray colors. Moreover, we re-emphasize that the darker gray pixels are associated with more developed chaos in the given models. Note that some stability windows are known as "shrimps" due to their shape. Such
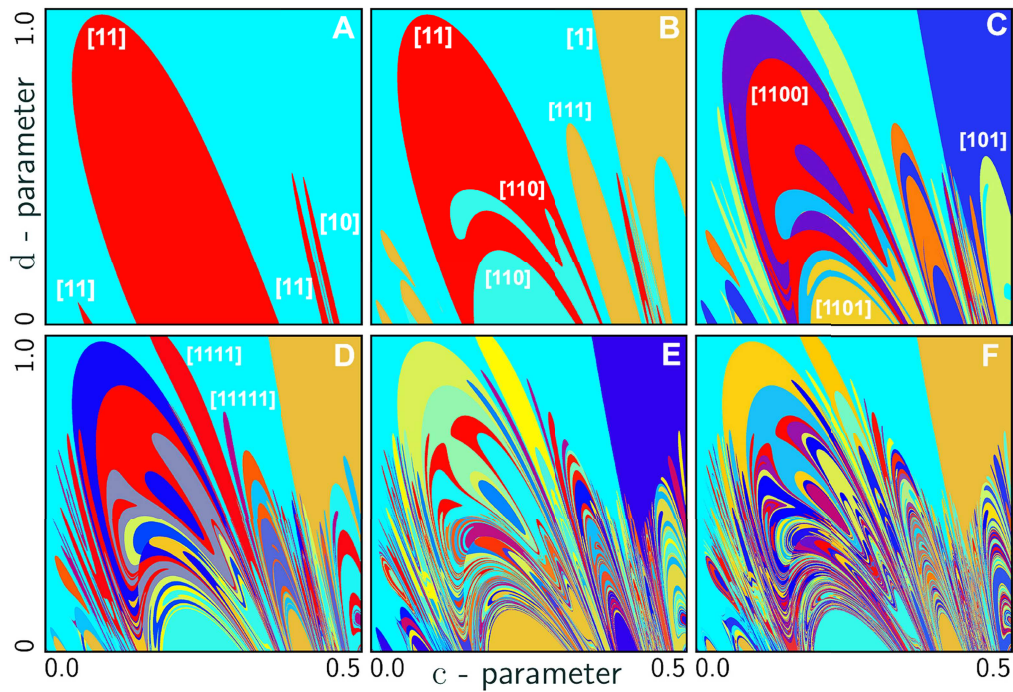
FIG. 24. The (c, d)-parameter sweeps of the cubic ACST-model to disclose the combined bifurcation unfoldings with self-similar, scaled-down organization, due to a plethora of homoclinic orbits in its phase space; compare with Fig. 21 using the original parameters and the sweeps of the Chua circuit in Figs. 16(b) and 19. Panels (a)–(f) are obtained using symbolic sequences [3,3]- through [3,8].
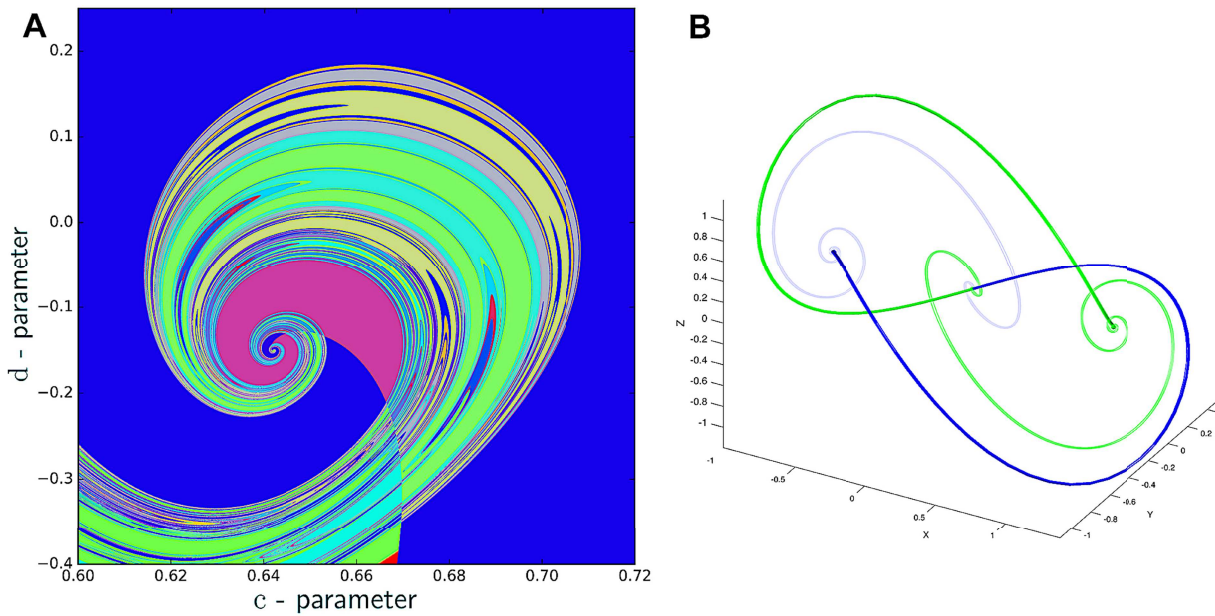

FIG. 25. (a) The (c, d)-parameter sweep of the cubic ACST-model to reveal the primary T-point corresponding to the heteroclinic connection, $[1000, \ldots, \infty]$ connecting the saddle-focus $O(0, 0, 0)$ of (2,1)-type with the saddle-foci O_1 (and O_2 due to the symmetry) of (1,2)-type in the phase space of the cubic ACST-model at $(c, d) \simeq (0.642, -0.15)$ as panel (b) depicts; compare with Fig. 21 using the original parameters and the sweeps of the Chua circuit in Figs. 16(b) and 20.
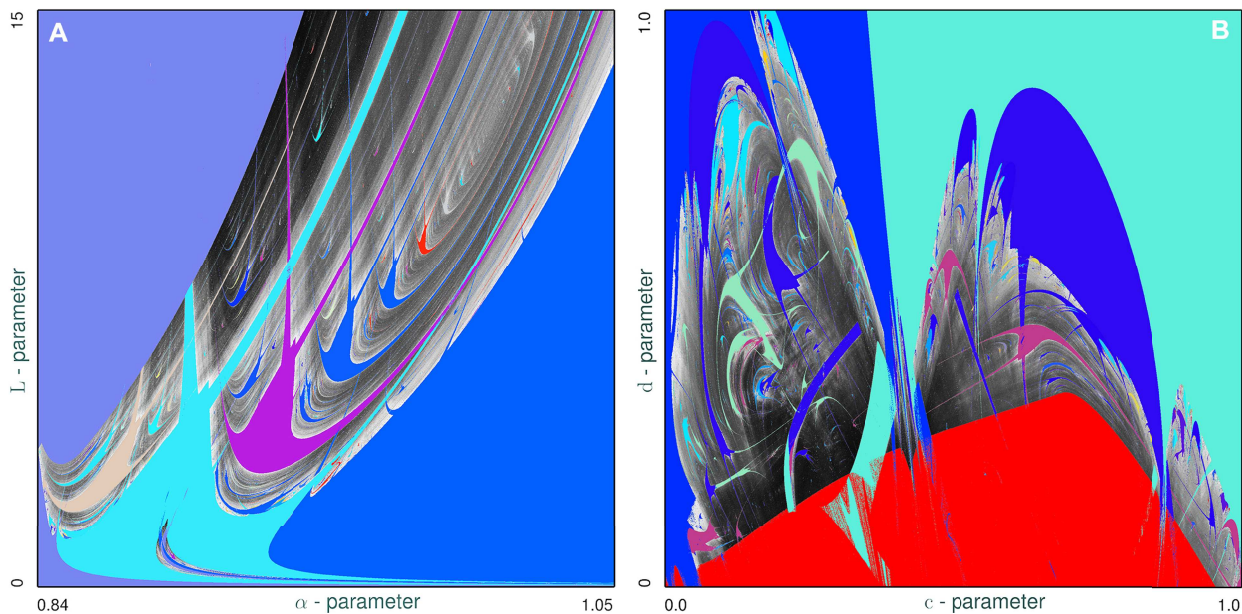
FIG. 26. Long [601–1000]-symbol DCP-sweeps on a 5000 × 5000-size grid to reveal stability windows (also known as "shrimps") (in solid colors) due to saddle-node bifurcations of periodic orbits and chaos-land (grayish regions—with darker gray implying greater complexity) due to the Shilnikov saddle-focus in the parameter space of the Chua circuit (a) and the cubic ACST-model (b) with the transformed parameters. In the red region in (b), the solutions of the ACST-model run to infinity.

a shrimp is formed by transverse saddle-node bifurcations of periodic orbits that are typically caused by homoclinic tangencies due to spiraling saddle-foci in these and other systems. In the blue regions on opposite sides in Fig. 26(a), the binary sequences for the separatrix Γ_1 include periodic blocks $\{\overline{1}\}$ and $\{\overline{10}\}$, respectively. While $\{\overline{1}\}$ may correspond to a stable equilibrium state O_1 and stable periodic orbits around it or even a chaotic attractor emerging through a period-doubling cascade of the former, the block $\{\overline{10}\}$ may be associated with various symmetric and asymmetric stable figure-8 periodic orbits. In Fig. 26(b), red color marks the region where the trajectories escape to infinity.

VII. CONCLUSIONS AND DISCUSSIONS

We developed a general theory of homoclinic bifurcations of the Shilnikov saddle-focus in $\mathbb{Z}_2$-symmetric systems. It discloses the ordered intricacy of corresponding structures and their organization in the bifurcation unfoldings of such systems, including the scalability ratio $e^{-\frac{2\pi}{\Omega_0}}$ of the width and distance between two sequentially close l- and $(l+1)$-homoclinic orbits.

The theoretical foundations were implemented using a novel algorithm of symbolic, binary description to examine and demonstrate the universal organization of Shilnikov homoclinic bifurcations in two symmetric systems: the smooth Chua circuit and the cubic asymptotic normal form—the Arneodo–Coullet–Spiegel–Tresser model.

We demonstrated how recently developed toolkit, Deterministic Chaos Prospector with GPU parallelization, can quickly reveal the regions of simple and chaotic dynamics in the parameter space

of the selected models. One of the objectives of this paper is to showcase our know-how with an open source GPU-based computational toolkit based on the symbolic framework that should be broadly accessible (see below) and practical for the nonlinear dynamics community to analyze homoclinic bifurcations and structural in/stability in various systems.

The theory and the methodology created in this study can further advance new theoretical ideas and computational approaches for a better understanding of the origin and the universal structure of deterministic chaos in full generality, including diverse applications from mathematical, physical, and biological sciences.

DATA AVAILABILITY

The DCP code used in this study is open source and freely available in Bitbucket at https://bitbucket.org/pusuluri_krishna/deterministicchaosprospector, Ref. 66.

REFERENCES

[1] L. P. Shilnikov, "A case of the existence of a denumerable set of periodic motions," Dokl. Akad. Nauk SSSR **160**, 558–561 (1965).

[2] L. P. Shilnikov, "The existence of a denumerable set of periodic motions in four-dimensional space in an extended neighborhood of a saddle-focus," Sov. Math. Dokl. **8**(1), 54–58 (1967).

[3] L. P. Shilnikov, "On the birth of a periodic motion from a trajectory bi-asymptotic to an equilibrium state pf the saddle type," Sov. Math. Sb. **35**(3), 240–264 (1968).

[4] L. P. Shilnikov, "A contribution to the problem of the structure of an extended neighborhood of a rough equilibrium state of saddle-focus type," Math. USSR-Sb. **10**, 91–102 (1970).

[5] S. V. Gonchenko, D. V. Turaev, P. Gaspard, and G. Nicolis, "Complexity in the bifurcation structure of homoclinic loops to a saddle-focus," Nonlinearity **10**, 409 (1997).

[6] V. Gonchenko and L. Shilnikov, "On bifurcations of systems with homoclinic loops to a saddle-focus with saddle index 1/2," Dokl. Math. **76**, 929–933 (2007).

[7] R. Barrio, A. Shilnikov, and L. Shilnikov, "Kneadings, symbolic dynamics and painting Lorenz chaos," Int. J. Bifurcation Chaos **22**, 1230016 (2012).

[8] R. Barrio, F. Blesa, S. Serrano, T. Xing, and A. L. Shilnikov, "Homoclinic spirals: Theory and numerics," in *Progress and Challenges in Dynamical Systems* (Springer, 2013), pp. 53–64.

[9] T. Xing, R. Barrio, and A. L. Shilnikov, "Symbolic quest into homoclinic chaos," Int. J. Bifurcation Chaos **24**, 1440004 (2014).

[10] K. Pusuluri, A. Pikovsky, and A. Shilnikov, "Unraveling the chaos-land and its organization in the Rabinovich system," in *Advances in Dynamics, Patterns, Cognition* (Springer, 2017), pp. 41–60.

[11] E. Lorenz, "Deterministic nonperiodic flow," J. Atmos. Sci. **20**, 130–141 (1963).

[12] L. Shilnikov, "Bifurcation theory and the Lorenz model," in *The Hopf Bifurcation and Its Applications*, Appendix to Russian ed., edited by J. Marsden and M. McCraken (Elsevier, 1980), pp. 317–335.

[13] A. Shilnikov, "Bifurcations and chaos in the Morioka-Shimizu model. Part I," in *Methods in Qualitative Theory and Bifurcation Theory* (Elsevier, 1986), pp. 180–193 (in Russian).

[14] A. L. Shilnikov, "On bifurcations of the Lorenz attractor in the Shimizu-Morioka model," Physica D **62**, 338–346 (1993).

[15] A. L. Shilnikov, L. P. Shilnikov, and D. V. Turaev, "Normal forms and Lorenz attractors," Int. J. Bifurcation Chaos **3**, 1123–1139 (1993).

[16] K. Pusuluri and A. Shilnikov, "Homoclinic chaos and its organization in a nonlinear optics model," Phys. Rev. E **98**, 040202 (2018).

[17] K. Pusuluri and A. L. Shilnikov, "Symbolic representation of neuronal dynamics," in *Advances on Nonlinear Dynamics of Electronic Systems* (World Scientific, 2019), pp. 97–102.

[18] K. Pusuluri, H. Ju, and A. L. Shilnikov, "Chaotic dynamics in neural systems," in *Encyclopedia of Complexity and Systems Science*, edited by R. A. Meyers (Springer, Berlin, 2020), pp. 1–13.

[19] K. Pusuluri, H. G. E. Meijer, and A. L. Shilnikov, "Homoclinic puzzles and chaos in a nonlinear laser model," J. Commun. Nonlinear Sci. Numer. Simul. **93**, 105503 (2021).

[20] V. S. Afraimovich, V. V. Bykov, and L. P. Shilnikov, "The origin and structure of the Lorenz attractor," Sov. Phys. Dokl. **22**, 253–255 (1977).

[21] V. S. Afraimovich, V. V. Bykov, and L. P. Shilnikov, "On the origin and structure of the Lorenz attractor," Akad. Nauk. SSSR Dokl. **234**, 336–339 (1977).

[22] V. S. Afraimovich and L. P. Shilnikov, "Strange attractors and quasiattractors," in *Nonlinear Dynamics and Turbulence* (Pitman, 1983).

[23] L. P. Shilnikov and A. L. Shilnikov, "Shilnikov bifurcation," Scholarpedia **2**, 1891 (2007); see http://www.scholarpedia.org/article/Shilnikov_bifurcation, revision #153014.

[24] L. P. Shilnikov, "A certain new type of bifurcation of multidimensional dynamic systems," Dokl. Akad. Nauk SSSR **189**, 59–62 (1969).

[25] V. S. Afraimovich, S. V. Gonchenko, L. M. Lerman, A. L. Shilnikov, and D. V. Turaev, "Scientific heritage of L.P. Shilnikov," Regul. Chaotic Dyn. **19**, 435–460 (2014).

[26] L. P. Shilnikov, A. L. Shilnikov, D. V. Turaev, and L. O. Chua, *Methods of Qualitative Theory in Nonlinear Dynamics*, World Scientific Series on Nonlinear Science, Series A (World Scientific, 1998, 2001), Vol. 5, Parts I and II.

[27] V. I. Arnold, V. Afrajmovich, Y. S. Il'yashenko, and L. P. Shilnikov, *Dynamical Systems V: Bifurcation Theory and Catastrophe Theory* (Springer Science & Business Media, 2013), Vol. 5.

[28] P. Gaspard, "Generation of a countable set of homoclinic flows through bifurcation," Phys. Lett. A **97**, 1–4 (1983).

[29] L. Belyakov, "Bifurcation of systems with homoclinic curve of a saddle-focus with saddle quantity zero," Math. Notes **36**, 838–843 (1984).

[30] I. Ovsyannikov and L. P. Shilnikov, "On systems with a saddle-focus homoclinic curve," Mat. Sb. **172**, 552–570 (1986).

[31] I. Ovsyannikov and L. P. Shilnikov, "Systems with a homoclinic curve of multidimensional saddle-focus type, and spiral chaos," Math. USSR-Sb. **73**, 415 (1992).

[32] A. Arneodo, P. Coullet, and C. Tresser, "Possible new strange attractors with spiral structure," Commun. Math. Phys. **79**, 573–579 (1981).

[33] P. Gaspard and G. Nicolis, "What can we learn from homoclinic orbits in chaotic dynamics?," J. Stat. Phys. **31**, 499–518 (1983).

[34] P. Gaspard, R. Kapral, and G. Nicolis, "Bifurcation phenomena near homoclinic systems: A two-parameter analysis," J. Stat. Phys. **35**, 697–727 (1984).

[35] R. O. Medrano-T., M. S. Baptista, and I. L. Caldas, "Basic structures of the Shilnikov homoclinic bifurcation scenario," Chaos **15**, 033112 (2005).

[36] A. Fowler and C. Sparrow, "Bifocal homoclinic orbits in four dimensions," Nonlinearity **4**, 1159 (1991).

[37] A. Arneodo, F. Argoul, J. Elezgaray, and P. Richetti, "Homoclinic chaos in chemical systems," Physica D **62**, 134–169 (1993).

[38] V. V. Bykov, *Orbit Structure in a Neighborhood of a Separatrix Cycle Containing Two Saddle-Foci*, American Mathematical Society Translations: Series 2 (American Mathematical Society, 2000), Vol. 20, pp. 87–95.

[39] U. Feudel, A. Neiman, X. Pei, W. Wojtenek, H. Braun, M. Huber, and F. Moss, "Homoclinic bifurcation in a Hodgkin-Huxley model of thermally sensitive neurons," Chaos **10**, 231–239 (2000).

[40] S. Nicolay, F. Argoul, M. Touchon, Y. d'Aubenton Carafa, C. Thermes, and A. Arnéodo, "Low frequency rhythms in human DNA sequences: A key to the organization of gene location and orientation?," Phys. Rev. Lett. **93**, 108101 (2004).

[41] R. Barrio, F. Blesa, S. Serrano, and A. L. Shilnikov, "Global organization of spiral structures in biparameter space of dissipative systems with Shilnikov saddle-foci," Phys. Rev. E **84**, 035201 (2011).

[42] M. T. Koper, P. Gaspard, and J. Sluyters, "Mixed–mode oscillations and incomplete homoclinic scenarios to a saddle focus in the indium/thiocyanate electrochemical oscillator," J. Chem. Phys. **97**, 8250–8260 (1992).

[43] M. Bassett and J. Hudson, "Shilnikov chaos during copper electrodissolution," J. Phys. Chem. **92**, 6963–6966 (1988).

[44] C. Toniolo, G. Russo, S. Residori, and C. Tresser, "A phenomenological approach to normal form modeling: A case study in laser induced nematodynamics," Int. J. Bifurcation Chaos **15**, 3547–3566 (2005).

[45] J. M. Cortes, M. Desroches, S. Rodrigues, R. Veltz, M. A. Muñoz, and T. J. Sejnowski, "Short-term synaptic plasticity in the deterministic Tsodyks–Markram model leads to unpredictable network dynamics," Proc. Natl. Acad. Sci. U.S.A. **110**, 16610–16615 (2013).

[46] S. Malykh, Y. Bakhanova, A. Kazakov, K. Pusuluri, and A. L. Shilnikov, "Homoclinic chaos in the Rössler model," Chaos **30**, 113126 (2020).

[47] W. Barnett, G. Bella, T. Ghosh, P. Mattana, and B. Venturi, "Shilnikov chaos, low interest rates, and new keynesian macroeconomics," MPRA Paper No. 98417 (2020); see https://mpra.ub.uni-muenchen.de/98417/.

[48] S. V. Gonchenko, L. P. Shil'nikov, and D. V. Turaev, "Dynamical phenomena in systems with structurally unstable Poincaré homoclinic orbits," Chaos **6**, 15–31 (1996).

[49] S. Gonchenko, L. P. Shil'nikov, and D. Turaev, "Quasiattractors and homoclinic tangencies," Comput. Math. Appl. **34**, 195–227 (1997).

[50] D. Turaev and L. P. Shilnikov, "An example of a wild strange attractor," Sb. Math. **189**(2), 291–314 (1998).

[51]D. Turaev and L. Shil'nikov, "Pseudohyperbolicity and the problem on periodic perturbations of Lorenz-type attractors," Dokl. Math. **77**, 17 (2008).

[52]T. Matsumoto, S. Tanaka, and L. Chua, "Simplest chaotic non-autonomous circuit," Phys. Rev. A **30**, 1155–1159 (1984).

[53]G. Ramirez-Avila and J. Gallas, "How similar is the performance of the cubic and the piecewise-linear circuits of Chua?," Phys. Lett. A **375**, 143–148 (2010).

[54]A. Tsuneda, "A gallery of attractors from smooth Chua's equation," Int. J. Bifurcation Chaos **15**, 1–49 (2005).

[55]A. I. Khibnik, D. Roose, and L. O. Chua, "On periodic orbits and homoclinic bifurcations in Chua's circuit with a smooth nonlinearity," Int. J. Bifurcation Chaos **3**(02), 363–384 (1993).

[56]V. V. Bykov, "Bifurcations leading to chaos in Chua's circuit," Int. J. Bifurcation Chaos **8**, 685–699 (1998).

[57]P. Coullet, C. Tresser, and A. Arneodo, "Transition to stochasticity for a class of forced oscillators," Phys. Lett. A **72**, 268–270 (1979).

[58]A. Arneodo, P. Coullet, and C. Tresser, "Occurrence of strange attractors in three-dimensional Volterra equations," Phys. Lett. A **79**, 259–263 (1980).

[59]A. Arneodo, P. Coullet, and C. Tresser, "Oscillators with chaotic behavior: An illustration of a theorem by Shilnikov," J. Stat. Phys. **27**, 171–182 (1982).

[60]A. Arneodo, P. Coullet, E. Spiegel, and C. Tresser, "Asymptotic chaos," Physica D **14**, 327–347 (1985).

[61]O. E. Rössler, "An equation for continuous chaos," Phys. Lett. A **57**, 397–398 (1976).

[62]V. V. Bykov, "On systems with separatrix contour containing two saddle-foci," J. Math. Sci. **95**, 2513–2522 (1999).

[63]V. V. Bykov, "On the structure of bifurcations sets of dynamical systems that are systems with a separatrix contour containing saddle-focus," in *Methods of Qualitative Theory of Differential Equations* (Gorky University, Russia, 1980), pp. 44–72 (in Russian).

[64]A. Algaba, M. Merino, F. Fernández-Sánchez, and A. J. Rodríguez-Luis, "Open-to-closed curves of saddle-node bifurcations of periodic orbits near a nontransversal T-point in Chua's equation," Int. J. Bifurcation Chaos **16**, 2637–2647 (2006).

[65]A. Lempel and J. Ziv, "On the complexity of finite sequences," IEEE Trans. Inf. Theory **22**, 75–81 (1976).

[66]Deterministic Chaos Prospector (DCP) toolkit: https://bitbucket.org/pusuluri_krishna/deterministicchaosprospector.